Leveraging a radar-based disdrometer network to develop a probabilistic precipitation phase model in eastern Canada

Alexis Bédard-Therrien[1], François Anctil[1], Julie M. Thériault[2], Olivier Chalifour[2], Fanny Payette[3], Alexandre Vidal[3] and Daniel F. Nadeau[1]

[1]Département de génie civil et de génie des eaux, Université Laval, Québec, QC, Canada
[2]Département des sciences de la Terre et de l'atmosphère, Université du Québec à Montréal, Montréal, QC, Canada
[3]Hydro-Québec, Direction Planification de la conduite du système énergétique, Montréal, QC, Canada

Correspondence to: alexis.bedard-therrien.1@ulaval.ca

Abstract. This study presents a probabilistic model that partitions the precipitation phase based on hourly measurements from a network of radar-based disdrometers in eastern Canada. The network consists of 27 meteorological stations located in a boreal climate for the years 2020–2023. Precipitation phase observations showed a 2-m air temperature interval between 0–4°C where probabilities of occurrence of solid, liquid, or mixed precipitation significantly overlapped. Single-phase precipitation was found to occur more frequently than mixed-phase precipitation. Probabilistic phase-guided partitioning (PGP) models of increasing complexity using random forest algorithms were developed. The PGP models classified the precipitation phase and partitioned the precipitation accordingly into solid and liquid amounts. PGP_basic is based on 2-m air temperature and site elevation, while PGP_hydromet integrates relative humidity, surface pressure and precipitation rate. PGP_full includes all previous data, along with atmospheric reanalysis data, the 1000-850 hPa layer thickness, and temperature lapse rate. The PGP models were compared to benchmark precipitation phase partitioning methods. These included a single temperature threshold model set at 1.5°C, a linear transition model with dual temperature thresholds of –0.38 and 5°C, and a psychrometric balance model. Among the benchmark models, the single temperature threshold had the best classification performance (F1 score of 0.74) due to a low count of mixed-phase events. The other benchmark models tended to over-predict mixed-phase precipitation in order to decrease partitioning error. All PGP models showed significant phase classification improvement by reproducing the observed overlapping precipitation phases based on 2-m air temperature. PGP_hydromet and PGP_full displayed the best classification performance (F1 score of 0.84). In terms of partitioning error, PGP_full had the lowest RMSE (0.27 mm) and the least variability in performance. The RMSE of the single temperature threshold model was the highest (0.40 mm) and showed the greatest performance variability. An input variable importance analysis revealed that the additional data used in the more complex PGP models mainly improved mixed-phase precipitation prediction. The improvement of mixed-phase prediction remains a challenge. Relative humidity was deemed the

least important input variable used, due to consistent near water vapour saturation conditions. Additionally, the reanalysis atmospheric data proved to be an important factor to increase the robustness of the partitioning process. This study establishes a basis for integrating automated phase observations into a hydrometeorological observation network and developing probabilistic precipitation phase models.

1   Introduction

Precipitation phase is a critical component in hydrological modelling. Simply put, the hydrological effect following either a snowfall or rainfall event is drastically different; snowfall accumulates in winter and melts later in the spring or during winter melt events, while rain can either infiltrate or become runoff, potentially increasing streamflow in the short term. The precipitation phase also affects snowpack characteristics in different ways; a rain-on-snow event infiltrates the snowpack, increasing its liquid water content, and can create ice layers and change the snowpack internal characteristics (Singh et al., 1997; Wever et al., 2016), while snowfall increases the depth of the snowpack. During individual precipitation events, errors in snowpack water equivalent (SWE) and depth are mainly caused by errors in precipitation partitioning (Leroux et al., 2023). On a seasonal basis, the precipitation phase significantly affects the ablation of the snowpack, particularly due to its impact on the snow albedo (Essery et al., 2013; Günther et al., 2019). As such, the cumulative effects of misclassified precipitation have a significant impact on various seasonal values such as peak SWE, peak discharge date, and snow cover duration (Harder and Pomeroy, 2014).

As the climate warms, regions that typically experience winter snowfall are expected to face more rainfall in their winter precipitation, resulting in more rain-on-snow events (Jeong and Sushama, 2018; Ye et al., 2008; Musselman et al., 2018). Consequently, the proportion of runoff caused by rain-on-snow events during the winter is projected to increase in these regions (Jeong and Sushama, 2018; Musselman et al., 2018). Effective precipitation partitioning methods are more important than ever to anticipate potentially damaging events and to monitor water resources at the catchment scale. This need is also felt for field monitoring of precipitation quantities. Indeed, solid precipitation is much more sensitive to undercatch (underestimation due to the wind moving hydrometeors away from the gauge) than liquid precipitation (Rasmussen et al., 2012). Consequently, an inaccurate identification of the phase necessarily translates into an erroneous estimation of the precipitation quantity. Ehsani and Behrangi (2022) showed that undercatch for solid precipitation introduced a significant bias in gridded precipitation products at both the seasonal and annual scales at higher latitudes. This highlights the need to account for the precipitation phase at the synoptic scale, especially when using precipitation products to bias-correct satellite precipitation estimates (Behrangi et al., 2019; Ehsani and Behrangi, 2022).

The modelling of the precipitation phase in operational hydrological models is often based on a single near-surface air temperature threshold (Harpold et al., 2017). While simple to implement, this method cannot predict mixed precipitation events, which tend to occur when falling hydrometeors of different sizes coexist and melt at different rates (Thériault and Stewart, 2010). As an alternative to the single-threshold approach, one can use a linear relationship to account for mixed-phase precipitation events that occur between those two thresholds. Furthermore, these types of methods can be refined into curvilinear functions, which would theoretically yield a more accurate phase identification (Feiccabrino et al., 2013). In both cases, the classification error is reduced when compared to the single threshold approach (Feiccabrino et al., 2013; Wen et al., 2013). The advantage of using temperature threshold-based models comes mainly from a data availability and computational requirement standpoint. Variables other than air temperature are known to influence the precipitation phase, such as relative humidity and atmospheric pressure (Behrangi et al., 2018; Dai, 2008; Jennings et al., 2018). Thus, precipitation partitioning models can be improved by using dew point temperature (e.g. Marks et al., 2013; Ye et al., 2013) or wet bulb temperature (e.g. Ding et al., 2014; Wang et al., 2019; Behrangi et al., 2018) instead of relying solely on air temperature, increasing the spatial robustness of such models.

Phase partitioning models tend to rely on near-surface hydrometeorological variables because this information is easily accessible. However, the hydrometeor's initial phase as it leaves the cloud, the shape and size distribution of the precipitation particles, and the properties of the atmosphere from the cloud to the ground all determine the precipitation phase (Feiccabrino et al., 2015). As they fall, the hydrometeors exchange latent and sensible heat with their surroundings, linking their phase to the temperature and vapour deficit as they fall through the atmosphere. Additionally, both heat fluxes are also affected by the ventilation of the hydrometeor, which depends on its fall speed and the surrounding wind velocities (Stewart, 1992).

Atmospheric temperature gradients can vary with time, so the thickness of the melting atmospheric layer is also a key variable to consider, as it affects the time the hydrometeor spends in conditions favourable to melting. Empirical models approximate this layer thickness by computing the height difference between two selected pressure levels (Feiccabrino et al., 2015). Precipitation rates can also increase the energy required to melt hydrometeors. Indeed, at high precipitation rates, there is a larger volume to melt, thus increasing the likelihood of solid precipitation at warmer temperatures (Froidurot et al., 2014; Thériault and Stewart, 2010). Therefore, by accounting for the characteristics of the atmospheric layer, microphysical models can determine the precipitation phase of falling hydrometeors (Thériault and Stewart, 2010). Other models are instead based on the statistical relationship between the hydrometeorological variables and the precipitation phase. Such models compute the probability of a precipitation phase occurring considering a set of environmental conditions.

The methodology for calculating the probability of phase occurrence varies across studies and includes, for example, a curvilinear function (Dai, 2008), logistic regression (Behrangi et al., 2018; Froidurot et al., 2014; Jennings et al., 2018), and machine learning algorithms (Shin et al., 2022). These methods output a precipitation type rather than a fraction of solid and liquid precipitation, in the case of dual threshold models. However, the use of these methods is limited when dealing with mixed-phase precipitation, as they do not provide information on how the precipitation is partitioned. Fortunately, mixed-phase events are less common than single-phase events (Dai, 2008) and are thus often omitted from studies using probabilistic methods.

In addition to selecting the appropriate variables to include in a phase partitioning model, the quality and availability of the validation dataset is a critical aspect to consider. Indeed, the scarcity of validation data was cited by Harpold et al. (2017) as a major factor hindering the development of phase partitioning models. Direct manual phase observations collected from trained observers have been used to validate precipitation partitioning models (e.g. Behrangi et al., 2018; Dai, 2008; Froidurot et al., 2014; Jennings et al., 2018). Jennings et al. (2023) have also shown the possibility of using crowdsourced precipitation phase data. While such datasets are extensive in time and space, they do not provide quantitative information on the snow and rain fractions in mixed-phase events, thus limiting the possible predicted precipitation phases to either solid or liquid.

High-frequency automatic measurements do not suffer from limitations caused by mixed-phase precipitation (Froidurot et al., 2014; Harpold et al., 2017), as the precipitation phase can be coupled with a concurrent precipitation amount. When both phase identification and precipitation gauge measurements are made at a high frequency, phase-separated precipitation can be compiled for hourly or shorter time steps, thus allowing for mixed-phase partitioning. One possible validation approach based on automatic data is to use precipitation measurements collocated with snow cover height measurements (Harder and Pomeroy, 2013; Marks et al., 2013). A more direct automatic approach is to use a disdrometer, which identifies the phase of the hydrometeor according to its size and falling speed. For instance, Wayand et al. (2016) utilized a disdrometer to associate precipitation phase with precipitation amounts, which helped evaluate multiple phase models. This combination of observations not only allows for the validation of a phase model, but also addresses a major limitation of previous studies, namely the partitioning of precipitation in the case of mixed-phase events. Another important factor to consider is the time step of the validation data. While many conceptual hydrological models employ daily time steps to determine precipitation phase, sub-daily time steps greatly enhance the accuracy of modelled phase (Feiccabrino, 2020; Harder and Pomeroy, 2013). Therefore, it is necessary to use sub-daily time steps, such as 15 minutes or hourly, as a significant portion of the phase model's performance depends on the time step of interest.

145   There are many ways to improve the representation of the precipitation phase for hydrological purposes. As pointed out in Harpold et al. (2017), the often too simple phase models need more hydrometeorological observations for a successful partitioning of the precipitation phase. Such observations include the relative humidity, as well as atmospheric information, like the temperature and humidity lapse rate. Additionally, an important research limitation comes from

150   the lack of validation data. Direct observations, while commonly utilized, have limited application for mixed phase precipitation due to their qualitative nature. A preferable solution involves automated phase observations, as they enable the coupling with precipitation rate measurements. However, direct phase observation datasets indicate the existence of a temperature transition zone, where both snow and rain are possible. This highlights the

155   limitations of simplistic phase models that fail to capture the complex nature of phase determination.

    This study leverages a unique regional-scale radar disdrometer network coupled with precipitation observations to develop a probabilistic phase partitioning model. The probabilistic model follows a phase-guided partitioning (PGP) in the form of a chain of random forest models.

160   The precipitation phase is classified before partitioning to accurately replicate its intricate behaviour and to take advantage of the significant amount of validation data available through such a network. As such, the models classify the precipitation as either solid, liquid, or mixed phase. The predicted phase then dictates the partitioning into solid and liquid fractions. Additionally, multiple PGP models with lower data requirements are developed to evaluate the

165   possibility of utilizing such models in practical operations. This study begins with a description of the precipitation dataset and hydrometeorological variables used, followed by the methodology used to develop the PGP models. Finally, the results section presents an analysis of the dataset and evaluates the model's phase classification and partitioning performance, comparing it to benchmark models of differing levels of complexity.

170 **2   Data**

2.1   Surface hydrometeorological measurements

    The disdrometer network used for this study was deployed on the north shore of the St. Lawrence River in the province of Quebec, Canada (Fig. 1). It is part of a larger hydrometeorological observation network operated by Hydro-Quebec, a public utility responsible for the generation

175   and distribution of electricity in Quebec. The network lies between latitudes 47.23 and 52.13 °N, and longitudes 63.17 to 75.29° W, spanning an area of roughly 532,594 km^2. The 27 stations have been in operation for varying periods of time between the years 2019 and 2023, totalling 80 site-years. The site elevations range from 315 to 641 m above sea level (ASL), for an average

of 469 m ASL. The names, coordinates, and operational timeframes for each station are presented in the Appendix A.

The sites have a mean annual 2-m air temperature of 0.2°C and a mean annual cumulative precipitation of 902 mm, calculated from 160 site-years of daily observations. Figure 2 illustrates the distribution of annual mean daily 2-m air temperature and precipitation, as well as the elevation of the sites. The annual precipitation decreases with latitude, as the northern sites (>51° N) experience an annual mean of 813 mm. The southernmost sites (<49° N) receive more precipitation on average, with an annual mean of 1002 mm. However, the variability observed at these sites is much greater than observed elsewhere. The sites' elevation follows mostly a normal distribution within a 400 m range of the mean, with elevations generally increasing northward. Following Köppen climate classification, the sites are nearly evenly split between humid continental (Dfb) and humid subarctic (Dfc) climates. The study period spans from October 1 to June 1 of the following year, as the chances of snowfall are practically non-existent outside of these dates for the domain of interest.

Each site is equipped with a radar-based disdrometer (model WS100, Lufft), providing 15-min phase identification. The WS100 is a K-band (24 GHz) Doppler radar that classifies droplets into 11 size classes between 0.3 and 5.0 mm. The disdrometer assigns World Meteorological Organization (WMO, table 4677) present weather codes for no precipitation (code 0), rain (code 60), freezing rain (code 67), mix of rain or drizzle and snow (code 69), and snowfall (code 70). The precipitation phase is identified according to the hydrometeor diameter-fall velocity relationships for water droplets outlined in Gunn and Kinzer (1949), as well as in Locatelli and Hobbs (1974) for solid-phase precipitation particles. Rain and snow falling velocity as a function of measured reflectivity from K-band Doppler radar was investigated in Atlas et al. (1973) and remains an area of active research (e.g. Garcia-Benadi et al., 2020; Kneifel et al., 2011; Löffler-Mang et al., 1999; Sarkar et al., 2015). For simplicity, the phase identification derived from the diameter-fall velocity relationships are referred as observations in this study. In addition, each site also provides measurements of SWE using a passive gamma ray monitoring system (model CS725, Campbell Scientific) and snow depth using an ultrasonic sensor (SD, model SR50A, Campbell Scientific).

The meteorological observations in this study come from weather stations operated by Hydro-Quebec and SOPFEU, the province's wildfire prevention organization. The weather stations provide 15-min accumulated precipitation (model Pluvio[2] by OTT, equipped with a single-Alter shield), allowing the coupling of precipitation with concurrent disdrometer phase identification. The weather stations measure hourly air temperature (model CS109, Campbell Scientific) and relative humidity (model HMP155a, Campbell Scientific) with sensors mounted at 2 m above

ground. Additionally, wind speed and direction are monitored at a 15-min interval with a ground
propeller anemometer (model 05103, Young) mounted 2 m and 10 m above ground.

Most of the study sites and weather stations are located in close proximity to each other. Specifically, 67% of the study sites are within 3 km of or collocated with the nearest weather station. The remaining stations are between a median distance of 7 km and a maximum distance of 12 km. The only exception is the AUXLOUPS station and the nearest weather station, which are separated by 28 km. To account for the elevation differences between the study sites and weather stations, the air temperature measurements were adjusted using international standard atmosphere methods. The discussion section will address the uncertainty related to the distance between the study site and the weather station. The temporal resolution and detailed specifications about the study sites' instruments are provided in Table 1.

2.2 Reanalysis products

Hourly atmospheric data from the ECMWF-ERA5 reanalysis (Hersbach et al., 2023) are added to this study's dataset, to account for the energy transfer to falling hydrometeors in the atmospheric levels closest to the surface. Furthermore, this will help assessing the potential performance gain of incorporating gridded data, despite the spatial scale discrepancy with local observational data. The added data include temperature profiles for pressure levels of 1000 and 850 hPa. The corresponding geopotential height of these levels is also added to the dataset. The values from the nearest $0.25° × 0.25°$ grid cell, roughly 28 km × 18 km at the study sites' latitude, are assigned to every study site. Additionally, the hourly surface atmospheric pressure from ERA5-Land (Muñoz Sabater, 2019) is added to the dataset, as it was not measured at the weather stations used in this study. The atmospheric pressure from the nearest 9 km × 9 km grid space is assigned to every study site. From this data, the thickness Δz between the 1000 and 850 hPa layers (m) is calculated with:

$$\Delta z = \frac{z_{850} - z_{1000}}{g} \tag{1}$$

where z_{850} and z_{1000} correspond to the geopotential heights ($m^2 \, s^{-2}$) at the top and bottom of the layer, and g is the gravitational acceleration ($9.81 \, m \, s^{-2}$). The layer thickness between the two pressure levels is correlated with the mean temperature of the layer and is also a commonly used variable in operational meteorological models (Feiccabrino et al., 2015). The pressure levels were selected based on their successful use in the classification of the precipitation phase at the surface in prior studies (e.g. Bourgouin, 2000; Shin et al., 2022). The temperature lapse rate Γ (°C km^{-1}) is also calculated:

$$\Gamma = -\frac{\Delta T}{\Delta z} \times 1000 \tag{2}$$

where ΔT correspond to the temperature difference between the 850 and 100 hPa layers (°C).

3 Methodology

3.1 Precipitation data processing

250 The observed 15-min precipitation amounts were compiled at the hourly time step. Each 15 min precipitation data segment was coupled with a disdrometer phase identification. Both valid, non-zero values were required for the data segment to be included in the analysis. A first filter was applied, where hourly precipitation rates < 0.2 mm h^{-1} were considered erroneous trace amounts, following standard WMO methodology (WMO, 2018). A second filter was also applied where

255 precipitation rates > 110 mm h^{-1} were considered erroneous (Smith et al., 2022). A neutral aggregating filter (Ross et al., 2020) was then applied to eliminate noise and diurnal oscillations in the precipitation data. Additionally, hourly precipitation exceeding 30 mm h^{-1} was visually inspected. Any data not consistent with nearby stations was considered invalid.

The disdrometers used in this study can identify freezing rain and a mix of rain and snow in

260 addition to snow and rain. However, as most hydrological models only interpret the effect of snow and rain, this study focuses on the prediction of solid and liquid precipitation. Therefore, the disdrometer identification of freezing rain and of mix of rain/drizzle and snow were aggregated, respectively with snow and rain events. For example, if an hourly precipitation has a fraction of rain and a mix of rain/drizzle and snow, it would be considered completely liquid

265 after the aggregation. The selected phase aggregation aims to group the phases that are most similar in terms of hydrological influence and average occurring temperature. These assumptions are supported by an analysis of the effect of each precipitation phase on the snowpack properties (height and snow water equivalent), as detailed in Appendix B.

When solid precipitation was identified, the universal transfer functions of Kochendorfer et al.

270 (2017) were applied to adjust for wind-induced gauge undercatch. To do so, local hourly wind speed and temperature measurements at gauge height were used, which were shown to provide appropriate corrections for sites in boreal climates (Pierre et al., 2019). The solid and liquid 15-min precipitation were then compiled at hourly time steps and partitioned into liquid and solid precipitation fractions, totalling 31,905 data points. The resulting phase partitioning was used to

275 classify the phase of each precipitation event as solid, liquid, or mixed, with respective dataset proportions of 71%, 22% and 7%.

Figure 3a shows the phase occurrence of the coupled 15-min precipitation data along an interpolated 15-min 2-m air temperature. The phase occurrence in Fig. 3b shows that it is mostly the mixed and liquid precipitation that are affected by the aggregation, and that very few freezing

280 rain events aggregated with snow events result in the snow and solid phase distributions being

very similar. The aggregation of the mix of rain/drizzle and snow with rain results in an increase in liquid precipitation in the 0–5°C range. Mixed-phase precipitation occurs in the same air temperature range as that of the mix of rain/drizzle and snow, suggesting that this phase is often present in mixed-phase precipitation, thus validating the aggregation. A cursory analysis of the mixed-phase precipitation events revealed that events with a phase transition between snow and mix of rain/drizzle and snow account for roughly 75% of the mixed-phase events. Transitions from rain to snow are infrequent and represent roughly 15% of the mixed-phase precipitation events, while the remainder includes other phase combinations.

3.2   Model performance evaluation

The models presented in this study are evaluated for their ability to correctly predict the precipitation phase using a variety of performance metrics. First, the metrics used to quantify the predictive ability of the models are the precision (PRE) and the recall (REC), as well as the F1 score (Rokach et al., 2023). The combination of precision and recall is commonly used to evaluate model classification performance, as the metrics indicate different information. The precision indicates the proportion of correct predictions for a given phase, while the recall indicates the probability of detection for a given phase. By definition, model precision and recall are inversely proportional. The assessment of both metrics informs if a model over or underpredicts a given class. For instance, low precision and high recall indicate a class overprediction, while high precision and low recall indicate a class underprediction. Therefore, a model that achieves good performance in both metrics is desirable.

$$PRE = \frac{TP}{TP + FP} \tag{3}$$

$$REC = \frac{TP}{TP + FN} \tag{4}$$

where TP, FN, FP are the true positive, false negative and false positive counts respectively for a given phase. The F1 score, being the harmonic mean of the precision and recall, is a useful metric to quantify the general performance of the model.

$$F1 = 2 \left(\frac{PRE \times REC}{PRE + REC} \right) \tag{5}$$

These metrics are computed for each precipitation phase separately. A general score is also computed by weighing each phase's score according to its proportion in the dataset. As such, the weighted F1 score is used as a general classification performance metric, as it combines both

precision and recall, and harshly penalizes a poor score in either of them while also considering the dataset imbalance.

Second, the model partitioning performance is evaluated based on the predicted solid and liquid precipitation amounts. The metrics used are the coefficient of determination R^2 and the RMSE. Due to the slightly asymmetric phase distribution and overlap between the phases shown in Fig. 3, different R^2 are calculated for the solid and liquid precipitation. Thereby, the metrics are calculated on the phase-separated precipitation rather than on the precipitation fraction, as the precipitation phase could be solid, liquid or mixed for a given temperature. Because of the partitioning between solid or liquid precipitation, the RMSE is equal to the root mean squared of the misclassified precipitation. Therefore, the RMSE is the same for both solid and liquid precipitation, and a single score is presented. Finally, the partitioning performance metrics are performed on different subsets of the dataset using a K-fold method. The K-fold validation method is commonly used to assess the variability of model performance with machine learning methods. By using different subsets of the dataset to train and validate the model K times, a more general performance can be assessed. Because of the fewer liquid and mixed precipitation events compared to solid precipitation events, the K-Fold is also stratified to maintain phase proportions between training and validation sets from fold to fold. As such, in the case of the partitioning validation, the variability of the precipitation amounts from fold to fold must be considered. The performance metrics are repeated until the variance of the partitioning performance metrics stabilizes. In this case, the validation was performed with 5-fold validation and was repeated six times for a total of 30 validation folds.

3.3   Phase-guided probabilistic precipitation phase model

Machine learning algorithms are powerful tools for building classification and regression models. Random forests (Breiman, 2001) are commonly utilized in the environmental sciences due to their simple implementation and lower susceptibility to overfitting compared to other models. The model is based on decision trees, where variables are randomly chosen at each node to create a prediction. Therefore, the decision trees, each unique due to randomness, provide predictions that are ultimately aggregated to generate a final well-informed prediction.

Given the overlapping phases of the data set, a Random Forest (RF) classifier is used to predict the precipitation phase with a probabilistic approach. The procedure to develop the RF model is illustrated in Fig. 4. To address the phase type imbalance, the data were adjusted by undersampling the solid phase and increasing the weight of both liquid and mixed precipitation phases in the dataset. To achieve this, only data points with air temperatures between –4 and 8°C were kept in the analysis. The phase proportions resulting from the undersampling are 60% solid, 26% liquid and 14% mixed. The data were then split using an 80/20 ratio between the training and validation sets respectively, resulting in 13,339 data points for training and 3,335 for

350   validation. To account for the prevalence of solid precipitation samples, the training and validation sets were stratified to maintain the aforementioned phase proportions between the two subsets (60% solid, 26% liquid, 14% mixed). Hyperparameters were optimized on the training set to increase the model performance and reduce the chance of overfitting by using a stratified 5-fold cross validation and maximizing for a weighted F1 score. The RF classifier was then

355   retrained on the entire training data set and was ready for use on the validation set.

While the precipitation partitioning is straightforward when the predicted phase is either solid or liquid, it is less so for predicted mixed phase, where a solid and liquid precipitation fraction must be assigned. Thus, in the case of a predicted mixed phase, an RF regression model is developed following the same steps described above. The loss function used to optimize the

360   regression model parameters is the mean-squared error (MSE), to increase the penalty on larger errors. The Phase-Guided-Partitioning model predicts a precipitation phase, as well as a solid and liquid precipitation partitioning according to the predicted phase, with the complete process illustrated in Fig. 5.

Multiple PGP models using a combination of atmospheric variables were developed. The subsets

365   of input variables of the PGP models accommodate different levels of data availability, ranging from the strictest minimum data requirements (e.g., in an operational context) to atmospheric variables, with each subset fully incorporating the previous subsets (see Table 2). This approach will help to quantify the impact of some atmospheric variables that are not measured at surface weather stations. The simplest model, PGP_basic, includes only 2-m air temperature and site

370   elevation. Next, PGP_hydromet includes all related near-surface hydrometeorological data, such as relative humidity, atmospheric pressure, and precipitation rate. Finally, the PGP_full model, as discussed in the previous sections, incorporates atmospheric data from reanalysis, specifically the thickness of the 1000-850 hPa layer and temperature lapse rate.

3.4   Benchmark phase partitioning models

375   The benchmark models used for this study are common methods of increasing complexity found in hydrological models. First, a single 2-m air temperature threshold (ST) model is used as a baseline comparison. This model separates precipitation into solid and liquid phases based on a calibrated air-temperature threshold. While this type of model is widely used, it is generally associated with larger partitioning errors on a seasonal basis (Harpold et al., 2017). Second, a

380   linear transition (LT) model is used. It allows for mixed-phase precipitation, while still being of low complexity. LT partitions the solid and liquid precipitation according to a linear relationship between a snow and rain temperature threshold. Finally, the psychrometric energy balance (PB) model is used, which is a phase partitioning method based on the mass energy and energy balance of a sublimating ice sphere that integrates the relative humidity to estimate the

385   hydrometeor temperature (Harder and Pomeroy, 2013). The estimated hydrometeor temperature is then used as an input in a two-parameter curvilinear relationship. All three benchmark models are calibrated individually with the least squares method, minimizing the error with the observed solid-phase fractions. The models and their calibrated values are given in Appendix C. The precipitation phase can then be inferred from the predicted fractions. In other words, mixed phase

390   will be predicted in the instance of non-zero solid and liquid fractions, otherwise the predicted phase is either solid or liquid. Previous studies that employed probabilistic models based on direct phase observations (e.g. Behrangi et al., 2018; Jennings et al., 2018) were not included as benchmark models. Mixed-phase precipitation is typically excluded from such studies, as there is no effective method to accurately partition the precipitation due to the categorical nature of

395   direct phase observations. The above considerations make such models difficult to compare with the PGP models presented in this study.

3.5 Input variable importance analysis

A common way to interpret input variable importance for a machine learning model is to use permutation importance, which helps decreasing the black-box aspect of machine learning

400   algorithms (McGovern et al., 2019). The performance of the model is computed according to a chosen scoring scheme. Each variable of the model is then shuffled individually. The goal of this step is to break the relationship between a variable and the desired prediction. After each shuffle, a performance score is calculated to show the decrease in model performance. This process is then repeated several times to account for data variability. Thus, the relative importance of each

405   input variable to the model can be quantified with the resulting performance decrease. Permutation importance analysis provides only the importance of an input variable to the model, not the inherent information provided by that variable. However, when shuffling a variable that is highly correlated to another, the model can still find the shuffled variable's information when performing permutation importance analysis. In practice, this is an important consideration as it

410   means the importance of either, or both, input variables can be lower. This analysis offers insight into the crucial variables for the PGP models and how they can be further improved.

4 Results

4.1 Dataset analysis

The distribution of the hydrometeorological variables categorized by precipitation phase is

415   displayed in Fig. 6. The temperature distributions show a significant overlap between all three phases from 1.5 to 3.6°C, similar to that reported in Jennings et al. (2023). Mixed precipitation probability peaks at approximately 2.4°C. The distribution of relative humidity reveals that precipitation is associated with near liquid water vapour saturation conditions, with a median

value of 97%, regardless of the precipitation phase. The mean precipitation rate is generally low, at 0.9 mm h^{-1}. The median precipitation rate for mixed-phase events is generally the highest at 0.8 mm h^{-1}, followed by liquid-phase events at 0.7 mm h^{-1} and solid-phase events at 0.6 mm h^{-1}. Atmospheric pressure distributions are similar for both liquid and mixed-phase precipitation events. The mean air pressure during the solid precipitation events is comparable to that of the other phases, but there are more events between 90 and 92 kPa. The distribution for the thickness of the 1000-850 hPa layer closely mirrors that of air temperature, given their general correlation. The temperature lapse rate averages 4.9°C km^{-1} and distributions, especially solid precipitation, show a bias toward the standard atmospheric lapse rate of 6.5°C km^{-1}.

The overlap of the phase distributions for each input variable, most notably the air temperature, indicates that a probabilistic approach is appropriate for predicting the precipitation phase. Indeed, between approximately 0 and 4°C, solid and liquid precipitation may occur separately or coexist. According to findings in previous studies, precipitation over land is more likely to occur in a single phase than in mixed phase precipitation (Dai, 2008; Froidurot et al., 2014), as is the case in this study, where only 13% of the precipitation data points are mixed phase. There is, however, a narrow 2-m air temperature range, between 2 and 2.5°C, where mixed-phase probability exceeds the probability of single-phase precipitation. An appropriate phase partitioning model must thus accurately predict the phase in the temperature interval where solid, liquid, and mixed precipitation occurrences overlap while also providing accurate partitioning when needed.

4.2   Phase classification

Figure 7 shows the phase density distribution of the benchmark models and the PGP models in comparison to the observations. The corresponding classification scores of the models, which were weighted to reflect the precipitation phase proportions in the dataset, are presented in Table 3. The phase density distributions show the limitations of benchmark phase partitioning models, namely that the mixed phase is absent or overrepresented compared to the observations. However, ST performs well in all three metrics due to the low likelihood of mixed phase occurrence. When evaluating the overall classification performance using the F1 score, LT follows ST because of a disparity between precision and recall that affects its F1 score. The lower recall score for LT can be attributed to its overprediction of the less frequent mixed phase, which, in turn, negatively affects the recall of other phases. This enhances the model's weighted precision by decreasing the number of false positives in non-mixed-phase prediction. The same reasoning can be more extensively applied to PB's weighted scores. The mixed phase's overlap with other phases significantly decreases the model's overall recall. Due to the relationships used to create the benchmark models, the overlap between all three phases is not accurately

represented. By including relative humidity, PB can model phase overlap, but this does not improve the modelled phase distribution density with respect to the observations.

The weighted F1 score for the PGP models shows that they have a more robust general performance, as they have high weighted precision and recall scores, while having a small disparity between both scores. The PGP models reproduce the observed phase overlap well, but slightly overpredict the mixed phase, affecting both the solid and liquid-phase predictions. PGP_basic exhibits the greatest mixed phase overprediction, while the difference between PGP_hydromet and PGP_full is marginal. This result suggests possible improvements to PGP models, particularly for mixed-phase precipitation.

The phase-separated classification metrics provide further insight into the performance of the models, shown in Fig. 8. The F1 score provides an overall performance for each phase prediction. PGP_full has the best F1 scores for both the solid and liquid phases, while PGP_hydromet has a higher F1 for the mixed phase. PGP_basic is generally the third best-performing model in terms of F1 score, except for the solid phase, where ST outperforms it. While it is not able to predict the mixed phase, ST has the highest scores for the liquid and solid precipitation phases out of the benchmark models. This is probably because mixed-phase precipitation events are only roughly 13% of the samples, this low proportion does not significantly decrease the model's performance. LT performs slightly worse than ST for both solid and liquid phases F1 scores but has the highest mixed-phase F1 score out of the benchmark models.

PB's poor F1 scores are explained by the overlaps between the phases shown in Fig. 7. The model allows the predicted mixed phase to overlap with the predicted solid and liquid phases, which is the opposite behaviour of the observed phase density, where mixed-phase precipitation mostly exist in the solid and liquid phase overlap. Given the modelled phase density and the resulting classification scores, the phase prediction ability of both LT and PB suffers from overprediction of the mixed phase. This is evidenced by the significant disparity between the precision and recall scores of LT and PB for the mixed phase. A high recall score signifies that the model minimizes the number of false negatives, which negatively affects the model's precision. Thus, overpredicting the mixed phase greatly reduces the models' precision for the mixed phase, while greatly increasing their recall for the mixed phase. Conversely, the conservative prediction of the liquid and solid phases increases the precision of the model but decreases the recall for both phases.

Although they are not always the best models in terms of either precision or recall, the PGP models have the best general performance, making them more reliable for phase prediction. Thus, PGP models significantly reduces phase identification error by showing high precision and recall, with small disparities for solid and liquid phase prediction. However, PGP's main

490   distinguishing feature is its general ability to predict mixed-phase precipitation. Furthermore, the disparity between the precision and recall scores for the mixed phase is much smaller than for the other models studied, indicating that the overprediction of the mixed phase is much less severe for PGP.

4.3   Precipitation partitioning

495   Figure 9 displays how the regression metrics vary across validation folds. The precipitation rate variability has a significant impact on ST's performance, making its ability to partition precipitation highly variable from winter to winter. In contrast, LT and PB exhibit better performance than ST due to their ability to partition the solid and liquid phases, with much less variability in performance. The variability of R^2 for liquid precipitation is lower for LT and PB

500   than for solid precipitation, because fewer of these events occur. For all regression metrics, LT and PB have similar performance. This is most likely due to the very humid environment, which decreases the difference between the 2-m air temperature and the hydrometeor temperature computed for PB.

The average regression metrics in Table 4 shows the partitioning performance of the various

505   models. All models have a high R^2 for solid precipitation, likely due to the abundance of solid precipitation. However, model performance decreases for liquid precipitation R^2, with ST being significantly lower than other models. This trend is also observed for the RMSE. While ST is the worst performing model, LT, PB and PGP_basic perform similarly in all regression metrics. The inclusion of hydrometeorological data in PGP_hydromet leads to a slight increase in

510   performance. Lastly, the inclusion of atmospheric data in PGP_full improves performance compared to the other models.

Generally, the performance of PGP_basic is similar to that of LT and PB, with slight differences. PGP_basic is more variable in its performance for solid precipitation R^2 and RMSE. This variability can be attributed to the misclassification of precipitation events due to its limited

515   input variables. The R^2 scores for PGP_hydromet are less variable than for PGP_basic, while its RMSE is the most variable out of the PGP models. PGP_full exhibits the lowest variability for both R^2 and is the only PGP model with RMSE variability similar to benchmark models LT and PB.

The broader RMSE score range of the PGP models highlights the impact of misidentified phases.

520   Misidentification can be more costly than for a benchmark model that systematically separates precipitation into solid and liquid phases for temperatures where mixed-phase events are possible. Furthermore, models such as LT and PB achieve partial accuracy in phase partitioning by forcing mixed-phase precipitation, but if a PGP model misclassifies the phase, the entire precipitation event may be incorrectly partitioned. However, PGP models do show that phase

525 identification prior to phase partitioning can reduce the overall error of a model for both solid and liquid precipitation. This suggests that improved phase identification, specifically with mixed-phase prediction, could greatly enhance the accuracy of precipitation partitioning from PGP models.

4.4 Input variable importance

530 Figure 10 shows the correlation matrix of PGP_full input variables. While the correlation of most input variable combinations is low, the 2-m air temperature and 1000-850 hPa layer thickness are highly correlated. The layer thickness is affected by environmental temperatures, as the air density is inversely proportional to its temperature. Therefore, as temperatures increase, the distance between two pressure levels also increase. There is a moderate negative

535 correlation between elevation and air pressure, probably because of the small range of study site elevations. The temperature lapse rate has a small correlation with almost all features.

The scoring scheme for permutation importance must be carefully selected according to the model and use case. In this instance, the PGP models tend to overpredict the mixed phase, which also negatively impact their ability to predict the other phases. In turn, this also affects the

540 models' partitioning error, which indicates that their overall performance is reliant on accurate phase classification. For these reasons, the chosen scoring scheme for the permutation importance is the weighted F1 score, to consider the classification of the imbalanced phase dataset.

Figure 11 shows the permutation importance of PGP_full input variables and the resulting

545 decrease in the weighted F1 score on the validation set. The 2-m air temperature is the most important variable, with its permutation decreasing the score by more than 0.2. The second most important variable is the 1000-850 hPa layer thickness, a result shared by Shin et al. (2022). Because of its high correlation with the 2-m air temperature, it is difficult to interpret the real importance of this variable. In terms of classification performance, the addition of this variable

550 seems to provide small improvements, as shown by the differences in classification metrics between PGP_hydromet and PGP_full.

For the remaining variables, the importance decreases sharply. However, while the individual importance of the variables is low, they improve the phase classification when combined. This suggests that the additional variables used in PGP_full likely improve mostly mixed-phase

555 prediction, which is supported by the model's performance in section 4.2. The elevation is used to approximate the atmospheric pressure of a site and can improve phase partitioning (e.g. Ding et al., 2014; Behrangi et al., 2018). Furthermore, atmospheric pressure is often cited as an important variable for phase partitioning (e.g. Behrangi et al., 2018; Dai, 2008; Jennings et al., 2018). The thinner air in low-pressure environments allows snow to reach the ground faster. The

560 temperature lapse rate provides key information regarding the amount of energy the hydrometeors absorb before reaching the ground.

The precipitation rate has a minor impact on the performance of the model. Nevertheless, it may hold significance for the prediction of the mixed phase. The precipitation rate is linked to the precipitation phase as it increases the energy required to completely melt falling precipitation
565 (Froidurot et al., 2014; Thériault et al., 2010). However, its effect is minimal, most likely due to the small proportion of mixed-phase events. Finally, the model ranks relative humidity as the least important feature. This outcome is unexpected because relative humidity was shown to have a significant effect on phase partitioning (e.g. Behrangi et al., 2018; Jennings et al., 2018). One explanation could be the high percentage of data points near water vapour saturation,
570 resulting in the variable being less regionally significant than more heterogeneous regions such as mountain ranges. Besides, this could account for the PB model's underwhelming classification accuracy since it utilizes relative humidity to determine the precipitation phase and the fact that it was developed for the drier climate near the Canadian Rockies.

5   Discussion

575 ### 5.1   Model performance and input variable importance

The classification and regression metrics of the PGP models show that phase classification prior to phase partitioning reduces the partitioning error of solid and liquid precipitation, while also providing a more reliable phase prediction than benchmark models. The use of radar-based disdrometer measurements enabled the partitioning step of the model by providing precipitation
580 fractions for mixed-phase events, a flaw mentioned in other studies (Froidurot et al., 2014; Jennings et al., 2018). Out of the benchmark models, ST displayed the best classification performance, despite not allowing for mixed-phase precipitation. The tendency of overpredicting mixed-phase precipitation of both LT and PB reduced their overall classification performance. This general behaviour was also observed in Leroux et al. (2023), where simpler
585 methods outperformed methods based on a precipitation phase fraction. However, ST showed significantly worse partitioning performance compared to LT and PB. The limitations of precipitation fraction-based models are highlighted by the fact that LT and PB were the worst performing phase classification benchmark models, despite being the best partitioning benchmark models. These models were calibrated to minimize partitioning error, but in doing
590 so, they are biased toward predicting mixed-phase precipitation. The mixed-phase prediction of the benchmark models could be artificially constrained to reduce overprediction and improve classification performance. Such constraints would, however, increase the benchmark models' partitioning error, given that they were calibrated according to solid precipitation fractions.

Therefore, there is a trade-off between classification and partitioning error for precipitation fraction-based models such as LT and PB.

PGP_basic, while showing an improvement in phase classification, did not significantly outperform the partitioning of benchmark models LT and PB. PGP_hydromet showed improved phase classification, notably for mixed phase, and partitioning. PGP_full showed further increase in overall performance, while also reducing the partitioning error variability. However, all PGP models tended to over predict the mixed phase as shown in Fig. 7. Reducing the overprediction of mixed phase is a persistent challenge in improving precipitation phase modelling, as noted in previous studies (Casellas et al., 2021; Leroux et al., 2023).

The permutation importance analysis showed that most input variables used, apart from the 2-m air temperature, are of low importance. However, the classification performance improvement of PGP_hydromet and PGP_full show the cumulative importance of the additional variables used, most notably for mixed-phase prediction. Despite many studies demonstrating its impact on precipitation phase, relative humidity was found to be the least important factor. This is likely due to the regional homogeneity, with most observations occurring near liquid water vapour saturation. The site elevation was considered important for phase classification, even though it is a constant variable. This suggests that an atmospheric pressure estimated by the elevation could provide enough information relevant to improve phase classification. Still, out of the hydrometeorological variables, the atmospheric pressure had the most impact on phase classification performance. This is in line with other studies that found it has a significant impact on the precipitation phase (e.g. Behrangi et al., 2018; Dai, 2008; Jennings et al., 2018), although generally to a lesser extent than relative humidity, when considering the regional variability.

The precipitation rate's low importance is most likely because it affects mixed-phase prediction, thus has low impact for overall performance. According to Thériault et al. (2010), higher precipitation rates raise the likelihood of larger hydrometeors, which require more energy to melt. Consequently, there is an increased likelihood of mixed-phase precipitation occurring in the form of partially melted hydrometeors. As noted by Feiccabrino et al. (2015), higher precipitation rates can lead to snowfall happening at warmer temperatures due to the presence of unstable air below the isothermal layer.

The permutation importance of 1000-850 hPa layer thickness is second to the 2-m air temperature. However, because of the high correlation of the pair of variables combined with the moderate classification improvement of PGP_full, the real importance of the 1000-850 hPa layer is most likely low. While the importance of the temperature lapse rate is low, the partitioning results demonstrated that incorporating gridded atmospheric variables alongside local observations led to a reduction in the variance of the regression performance. This finding is noteworthy because few studies, as pointed out by Harpold et al. (2017), have explored the

630   impact of incorporating atmospheric reanalysis data into phase modelling. Froidurot et al. (2014) indicated that models using atmospheric data did not greatly improve the phase prediction, as is the case in this study's classification performance. Furthermore, Dai (2008) emphasizes the terrain-dependent nature of lapse rates. Thus, even though the study sites in the region are relatively similar in terms of terrain, the importance of lapse rates in the modelling process was

635   still significant, contrary to the fairly homogenous relative humidity measurements.

5.2   Coupled precipitation data uncertainty

There are uncertainties regarding the results due to the dataset and assumptions employed. Hydrological models commonly limit the precipitation phases to solid or liquid. Nonetheless, this dataset includes a considerable quantity of mixed snow and rain/drizzle events, and it is

640   uncertain how hydrological models should handle this precipitation phase. The phase aggregation step considered the behaviour of the snowpack following the different phases detected by the disdrometers. Following a mix of rain/drizzle and snow, the SWE and snow height tended to decrease, a snowpack response similar to that following a rain event. It can be inferred that this type of precipitation is likely to be dominated by rainfall given the warm

645   temperature at which it occurs and the ensuing effects on the snowpack. However, it is probable that this interpretation is specific to the disdrometers used in this study unless evidence to the contrary emerges. However, phase identification errors have the potential to introduce uncertainties in the results, notably in the case of mixed-phase precipitation. To measure this uncertainty, it is recommended that studies be conducted using collocated WS-100 disdrometers

650   and other well-documented options such as laser disdrometers, to assess the differences between ground-truth providing instruments (Harpold et al., 2017).

Another source of uncertainty arises from the coupling of precipitation amounts and phase observations. Fehlmann et al. (2020) demonstrated that laser disdrometers have low missed event and false alarm rates for sub-daily integration times compared to precipitometers, but no

655   such study was conducted with the radar-based disdrometers of this study. Additionally, the study from Fehlmann et al. (2020) was carried out in a site sheltered from the wind, implying that the wind-induced gauge undercatch could not be studied. In turn, the wind could influence the missed event and false alarm rates of this study's instruments. In this study, data segments where either the precipitation gauge or disdrometer did not detect any precipitation were

660   discarded. Figure 12 displays the hit-rate of both the instruments at the initial 15-min intervals and shows that the instruments' hit-rates are generally in agreement. The instrument hits were normalized over the precipitation gauge observations to compute relevant agreement metrics. The precipitation gauge is considered as ground-truth as it would be used in conjunction with a precipitation phase model and phase observations are rare in operational context.

665   Precipitation data segments of 0.1 mm coincide with 38% of the disdrometer misses. Assuming that a significant portion of this precipitation data would be labelled as trace amounts when resampled at the hourly interval (< 0.2 mm), the probability of missed events is likely lower in reality. Multiple factors could account for disagreements between the instruments, including the effect of wind, which likely varies from instrument to instrument, and the fact that certain

670   stations are not collocated or nearby. However, the environmental effects on the disdrometer performance lacks previous studies and require more detailed investigation as outlined in Harpold et al. (2017).

Figure 13 shows the variation of the instrument agreement according to the distance between stations. The station pairs are divided into four distance categories: less than 3, 4 to 7, 7 to 12

675   and more than 12 km. Generally, the stations separated by less than 3 km show better agreement, with a few outliers. However, the instrument agreement does not seem to decrease with distance, as the 4 to 7 km category exhibits the poorest agreement. Notably, the AUXLOUPS station, separated by 28 km with the nearest weather station, has a probability of detection of 0.79, a false alarm rate of 0.14 and a miss rate of 0.21. These instrument agreement metrics are only

680   slightly worse than the metrics of the 15-min dataset in Fig. 12. This suggests that instrument agreement is linked to site specific conditions rather than distance between stations. However, by discarding data points where the instruments do not agree, we ensure that precipitation events are consistent across study sites and weather stations. In addition, the coupling of instruments from nearby stations brings the spatial scale of the observational data closer to the scale of the

685   reanalysis data.

5.3   Data validation across studies

The phase observations from this study can be compared to other studies that use different validation data, such as direct observations (e.g. Behrangi et al., 2018; Dai, 2008; Jennings et al., 2018). However, it can be difficult to compare the phase occurrence according to the 2-m air

690   temperature, as the datasets in such studies often exclude mixed-phase precipitation. Consequently, the mixed phase is usually not analyzed in detail. One method to simply compare phase partitioning models is the critical threshold air temperature value CT_a, which is defined as the critical temperature threshold where both solid and liquid phase have 50% chance of occurrence. In the case of this study, we define a different critical threshold for solid CT_S and

695   liquid phase CT_L, as well as a temperature where the probability for mixed phase is highest P_m. Figure 14 shows the probability of occurrence of the phases at the study sites separated in 0.2°C bins. The resulting thresholds are CT_S of 1.3°C, CT_L of 3.8°C and P_m of 2.4°C for a mixed-phase probability of 0.44. It is also noteworthy that P_m is roughly where the probability of solid and liquid precipitation is equal. Because of this study's aggregation step, CT_S should be similar to

700   CT_a values from other studies, as the aggregation mostly affected the probability of mixed and liquid precipitation, and CT_L will be much warmer than CT_a.

In Behrangi et al. (2018), the average hourly CT_a of 1.58°C aligns roughly with the study's CT_S and the calibrated 2-m air temperature threshold of benchmark ST. One of the main conclusions from the study was that the wet-bulb temperature model is more robust than the dry-bulb

705   temperature model, as the CT_a can vary significantly from site to site. Humid conditions lead to a cooler CT_a, while drier conditions have the opposite effect. As such, the CT_a for humid conditions would be approximately equal to the mean value minus the standard deviation, resulting in 1.18°C, and is thus closer to this study's CT_S of 1.3°C. Additionally, the upper limit of CT_a of 2.16°C in Behrangi et al. (2018) closely matches P_m. This finding lends credibility to

710   the disdrometer phase identification and the phase aggregation step, as it indicates the temperature range in which both solid and liquid phases are possible.

In Dai (2008), the overland 3-hourly CT_a of 1.2°C is comparable to this study's CT_S, despite the different time step. The chance for mixed phase in this study is much higher and more likely at warmer temperatures than that of Dai (2008), where they report a peak 14.3% chance of mixed

715   rain and snow at 1.4°C overland. However, Ding et al. (2014) have shown that the probability of mixed-phase precipitation at the daily time step greatly increases in humid conditions, particularly near saturation. Such an analysis would, however, be required at the hourly time step to confirm this behaviour. The reasoning for the increase in mixed-phase precipitation probability is that the increase in relative humidity decreases evaporative cooling and favours a

720   transition from snow to rain. In contrast, the temperature difference between the hydrometeors and the air decreases as humidity rises, which decreases sensible heat transfer and hinders the transition from snow to rain. The relatively homogenous conditions of the study sites could explain the differences in mixed-phase precipitation probability, while the analysis in Dai (2008) lumped together a large number of stations.

725   The findings in Jennings et al. (2018) report a much lower 3-hourly CT_a of 0.7°C for precipitation in 90–100% relative humidity and 0.9°C for precipitation occurring in 90–105 kPa, humidity and pressure conditions where the majority of this study's precipitation occur. The greater difference between these CT_a and CT_S could be due to several reasons. First, the 3-hourly CT_a should theoretically be lower than the hourly CT_a. As the time step increases, the occurrence

730   of mixed-phase precipitation increases due to the higher likelihood of a phase transition. Second, the different types of validation data could explain why CT_a is generally lower than CT_S. Phase identification errors, particularly near the solid-liquid phase transition, could also differ between direct observations and radar disdrometers.

Overall, the radar-based disdrometer measurements are similar to the findings of previous

735   studies, although with generally slightly warmer conditions of occurrence for solid precipitation.

However, more research is needed to properly quantify the uncertainties associated with this type of disdrometer. In addition, models based on automated phase observations may differ from those based on direct observations, especially as the time step can vary from study to study. This also highlights the importance of the verification step performed after aggregating mixed snow and rain/drizzle with rainfall, as their effect was deemed closer to that of rainfall.

6   Conclusion

The study used phase measurements from radar-based disdrometers to train probabilistic models to classify and partition precipitation data for a network of study sites in eastern Canada. The study sites were located in predominantly boreal climates and at similar elevations, ranging from 315 to 641 metres above sea level. The mean annual 2-meter air temperature was around 0.2°C, and the cumulative annual precipitation was significant at 902 mm. The humidity conditions for the data points used in the study were generally close to water vapour saturation. The utilization of automated measurements enabled partitioning of precipitation for mixed-phase events, which were previously limited with direct phase observations. The studied PGP models showed an improvement in phase partitioning with prior phase classification compared to benchmark models of varying complexity. PGP provides more accurate phase classification, which can benefit hydrological modelling at both local and watershed scales. It successfully reproduced the phase overlap between 1.5 and 3.5°C seen in Fig. 7, where mixed phase probability was the highest.

The classification performances show a substantial enhancement in phase classification as opposed to benchmark models, which were designed to minimize errors in phase partitioning. Additionally, the PGP models reduced partitioning error, especially PGP_hydromet and PGP_full. However, due to prior classification, partitioning performance is highly dependent on classification performance. As a result, the less complex PGP_basic had increased error variability. According to the input variable importance analysis, atmospheric pressure was the second most important near-surface variable for phase classification. The reanalysis atmospheric data reduced the partitioning error variability of PGP_full in comparison to the other PGP models. As for relative humidity, it was deemed to be the least important hydrometeorological feature for phase classification due to the regional homogeneity of the study sites. Overall, these findings demonstrate that automated phase observations enhance PGP method development and significantly improve precipitation phase classification, even with limited hydrometeorological information. The incorporation of reanalysis atmospheric data further enhances the accuracy of local observations, pointing toward potential operational applications for such methods.

The methodology of this study could be applied to other environments, including drier conditions or a broader spectrum of environments. Further research should include a comprehensive

comparison of the radar-based disdrometers used in this study with other phase validation techniques to assess potential limitations. Research is also needed to improve the prediction of the mixed phase. Other variables such as wind speed could be considered, as high wind speed can have a cooling effect on precipitation. Additionally, the impact of using a model that combines both phase classification and partitioning on snowpack accumulation and basin mass and energy dynamics should be investigated.

775

Appendix A. Study sites details

Table A1 shows the details for the study sites used from the Hydro-Québec observational network.

Appendix B. Disdrometer phase identification validation

Snow water equivalent (SWE) and snow depth observations were compiled from the entire network on a winter-by-winter basis. If more than 30% of a winter's snowpack observations were missing at a station, the winter is not included in this analysis. The resulting data subset consists of 11 winter-sites with a total of 53,520 hourly data points. The hourly data was then separated into precipitation events. The following filters were applied to the events:

- Duration ≥ 3 h,
- Mean 2-m air temperature between −5 and 5°C,
- Total precipitation ≥ 0.5 mm,
- Mean SWE ≥ 15 mm.

This filtering step aimed to exclude short events and events that occurred either in warmer conditions, where phases other than rain are uncommon, or in the absence of snow cover detectable by the instrumentation in place. As such, 235 precipitation events were retained. In addition to the data points encompassing each event, the following hours were added until the next update of the SWE observations, at most 6 hours. The events were then classified according to their main precipitation phase, that is the phase associated with at least half the total precipitation of the event.

The mean 2-m air temperature, SWE variation (ΔSWE), and snow depth variation (ΔSD) are compiled from precipitation events, according to the main precipitation phase of the event (Table B1). The effects of rain and the mix of rain/drizzle and snow events on the snowpack are similar, a SWE increase accompanied by a SD decrease. In addition, the average temperature of mixed snow and rain/drizzle events is significantly above the freezing point, where rainfall is more likely to occur than snowfall. In the case of freezing rain, the average temperature during the events is more similar to snowfall. Although freezing rain does not generally increase the SD, it contributes to the solid component of the snowpack as it freezes on contact. Thus, the phase aggregation of this study was based on the hydrological impact and temperature range of freezing rain and the mix of rain/drizzle and snow.

Appendix C. Benchmark models description

The single threshold model ST to compute the solid precipitation fraction f_{snow} (-) functions as follows:

810
$$f_{snow} = \begin{cases} 1 & T_a \leq T_K \\ 0 & T_a > T_K \end{cases} \tag{C1}$$

where T_a is the temperature (°C) and T_K is the calibrated temperature threshold (°C). The linear transition model LT uses two calibrated thresholds to calculate f_{snow}:

$$f_{snow} = \begin{cases} 1 & T_a \leq T_{snow} \\ \dfrac{T_{rain} - T_a}{T_{rain} - T_{snow}} & T_{snow} < T_a < T_{rain} \\ 0 & T_a \geq T_{rain} \end{cases} \tag{C2}$$

815

where T_{rain} and T_{snow} are the calibrated rain and snow thresholds (°C). Finally, the psychrometric energy balance model PB (Harder and Pomeroy, 2013) calculates f_{snow} as follows:

$$f_{snow} = \frac{1}{1+b+c^{T_i}} \tag{C3}$$

820

where b and c are calibrated values and T_i is the temperature of an unventilated hydrometeor (°C). Based on the mass balance of a sublimating ice sphere, T_i is calculated iteratively with the following function:

$$T_i = T_a + L_t \frac{D}{\lambda_t} \left(\rho_{T_a} - \rho_{T_i} \right) \tag{C4}$$

825

where L_t is the latent heat of sublimation or vaporization (J k^{-1}), D is the diffusivity of water vapour (m^2 s^{-1}), λ_t is the thermal conductivity of air (J m^{-1} s^{-1} K^{-1}) and ρ_{T_a}, ρ_{T_i} are the water vapour density of the surrounding air and on the hydrometeor's surface respectively (kg m^{-3}). The procedure to compute the variables is as detailed in Harder and Pomeroy (2013). D is

830 computed following Thorpe and Mason (1966):

$$D = 2.06 \times 10^{-5} \left(\frac{T_a}{273.15} \right)^{1.75} \tag{C5}$$

The vapour pressure e (kPa) is computed from Dingman (2015):

$$e = \frac{RH}{100} \times 0.611 \exp\left(\frac{17.37T}{237.3 + T} \right) \tag{C6}$$

835 where RH is the relative humidity (%) and T is the air temperature (°C). ρ is computed following the ideal gas law:

$$\rho = \frac{m_w e}{RT} \qquad (C7)$$

where m_w is the molecular weight of water (0.01801528 kg mol^{-1}) and R is the universal gas constant (8.31441 J mol^{-1} K^{-1}). The air thermal conductivity λ_t is computed from List (1951):

$$\lambda_t = 0.000063 T_a + 0.00673 \qquad (C8)$$

Finally, the latent heat of sublimation ($T_a < 0$) and vaporization ($T_a \geq 0$) are computed as follows (Yau and Rogers, 1996):

$$L_t = \begin{cases} 1000(2834.1 - 0.29T_a - 0.004T_a^2) & T_a < 0 \\ 1000(2501 - 2.361T_a) & T_a \geq 0 \end{cases} \qquad (C9)$$

Table C1 shows the calibrated parameters for the models presented in this section. The calibration was made on the same training set used for the PGP models. Figure C1 shows the simulated solid fraction for the benchmark models, as well as the observed solid fraction.

7 Data availability

The data used to train/calibrate the models in this study are available at 10.5281/zenodo.10790810. Supplementary data in the analysis are available from the corresponding author upon reasonable request. All data are subject to Hydro-Québec's Creative Commons Attribution—Non-Commercial 4.0 International licence (https://www.hydroquebec.com/documents-data/open-data/licence.html).

8 Author contributions

ABT, DFN, and FA designed research. FP and AV provided the study site data, as well as technical guidance. ABT with the help of OC performed data clean-up and corrections. ABT analyzed data and devised the precipitation partitioning models with inputs from DFN, FA, and JMT. ABT wrote the paper with inputs from DFN, FA, and JMT, as well as comments from OC, FP, and AV.

9 Competing interests

The authors declare that they have no conflict of interest.

10 Acknowledgements

This project was financially supported by the Quebec Ministry of Public Safety and by the Natural Sciences and Engineering Research Council of Canada through the Alliance program (grant ALLRP 549108 – 19 entitled, "Climate projection for hydrological applications in cold regions region, EVAP-2") with Hydro-Québec and Ouranos as industrial partners. We thank Dr. Feiccabrino and the two anonymous reviewers for their helpful comments and insight. We also thank M. Bédard-Therrien for their guidance in the development of machine learning models.

11 References

Atlas, D., Srivastava, R. C., and Sekhon, R. S.: Doppler radar characteristics of precipitation at vertical incidence, Reviews of Geophysics, 11, 1, https://doi.org/10.1029/RG011i001p00001, 1973.

Behrangi, A., Singh, A., Song, Y., and Panahi, M.: Assessing Gauge Undercatch Correction in Arctic Basins in Light of GRACE Observations, Geophysical Research Letters, 46, 11358-11366, https://doi.org/10.1029/2019GL084221, 2019.

Behrangi, A., Yin, X., Rajagopal, S., Stampoulis, D., and Ye, H.: On distinguishing snowfall from rainfall using near‐surface atmospheric information: Comparative analysis, uncertainties and hydrologic importance, Quarterly Journal of the Royal Meteorological Society, 144, 89-102, https://doi.org/10.1002/qj.3240, 2018.

Bourgouin, P.: A method to determine precipitation types, Weather and Forecasting, 15, 583-592, https://doi.org/10.1175/1520-0434(2000)015%3C0583:AMTDPT%3E2.0.CO;2, 2000.

Breiman, L.: Random forests, Machine learning, 45, 5-32, https://doi.org/10.1023/A:1010933404324, 2001.

Casellas, E., Bech, J., Veciana, R., Pineda, N., Rigo, T., Miró, J. R., and Sairouni, A.: Surface precipitation phase discrimination in complex terrain, Journal of Hydrology, 592, 125780, https://doi.org/10.1016/j.jhydrol.2020.125780, 2021.

Dai, A.: Temperature and pressure dependence of the rain‐snow phase transition over land and ocean, Geophysical Research Letters, 35, https://doi.org/10.1029/2008GL033295, 2008.

Ding, B., Yang, K., Qin, J., Wang, L., Chen, Y., and He, X.: The dependence of precipitation types on surface elevation and meteorological conditions and its parameterization, Journal of Hydrology, 513, 154-163, https://doi.org/10.1016/j.jhydrol.2014.03.038, 2014.

Dingman, S. L.: Physical hydrology, Third Edition, Waveland press, 2015.

895 Ehsani, M. R. and Behrangi, A.: A comparison of correction factors for the systematic gauge-measurement errors to improve the global land precipitation estimate, Journal of Hydrology, 610, 127884, https://doi.org/10.1016/j.jhydrol.2022.127884, 2022.

Essery, R., Morin, S., Lejeune, Y., and B Ménard, C.: A comparison of 1701 snow models using observations from an alpine site, Advances in Water Resources, 55, 131-148,
900 https://doi.org/10.1016/j.advwatres.2012.07.013, 2013.

Fehlmann, M., Rohrer, M., von Lerber, A., and Stoffel, M.: Automated precipitation monitoring with the Thies disdrometer: biases and ways for improvement, Atmospheric Measurement Techniques, 13, 4683-4698, https://doi.org/10.5194/amt-13-4683-2020, 2020.

Feiccabrino, J., Gustafsson, D., and Lundberg, A.: Surface-based precipitation phase determination
905 methods in hydrological models, Hydrology Research, 44, 44-57, https://doi.org/10.2166/nh.2012.158, 2013.

Feiccabrino, J., Graff, W., Lundberg, A., Sandström, N., and Gustafsson, D.: Meteorological knowledge useful for the improvement of snow rain separation in surface based models, Hydrology, 2, 266-288, https://doi.org/10.3390/hydrology2040266, 2015.

910 Feiccabrino, J. M.: Precipitation phase uncertainty in cold region conceptual models resulting from meteorological forcing time-step intervals, Hydrology Research, 51, 180-187, https://doi.org/10.2166/nh.2020.080, 2020.

Froidurot, S., Hingray, B., Zin, I., and Gautheron, A.: Sensitivity of Precipitation Phase over the Swiss Alps to Different Meteorological Variables, Journal of Hydrometeorology, 15, 685-696,
915 https://doi.org/10.1175/JHM-D-13-073.1, 2014.

Garcia-Benadi, A., Bech, J., Gonzalez, S., Udina, M., Codina, B., and Georgis, J.-F.: Precipitation type classification of micro rain radar data using an improved doppler spectral processing methodology, Remote Sensing, 12, 4113, https://doi.org/10.3390/rs12244113, 2020.

Gunn, R. and Kinzer, G. D.: The terminal velocity of fall for water droplets in stagnant air, Journal of
920 Meteorology, 6, 243-248, https://doi.org/10.1175/1520-0469(1949)006%3C0243:TTVOFF%3E2.0.CO;2, 1949.

Günther, D., Marke, T., Essery, R., and Strasser, U.: Uncertainties in Snowpack Simulations−Assessing the Impact of Model Structure, Parameter Choice, and Forcing Data Error on Point‐Scale Energy Balance Snow Model Performance, Water Resources Research, 55, 2779-2800,
925 https://doi.org/10.1029/2018WR023403, 2019.

Harder, P. and Pomeroy, J.: Estimating precipitation phase using a psychrometric energy balance method, Hydrological Processes, 27, 1901-1914, https://doi.org/10.1002/hyp.9799, 2013.

Harder, P. and Pomeroy, J. W.: Hydrological model uncertainty due to precipitation‐phase partitioning methods, Hydrological Processes, 28, 4311-4327, https://doi.org/10.1002/hyp.10214, 2014.

930 Harpold, A. A., Kaplan, M. L., Klos, P. Z., Link, T., McNamara, J. P., Rajagopal, S., Schumer, R., and Steele, C. M.: Rain or snow: hydrologic processes, observations, prediction, and research needs, Hydrology and Earth System Sciences, 21, 1-22, https://doi.org/10.5194/hess-21-1-2017, 2017.

Hersbach, H., Bell, B., Berrisford, P., Biavati, G., Horányi, A., Muñoz Sabater, J., Nicolas, J., Peubey, C., Radu, R., Rozum, I., Schepers, D., Simmons, A., Soci, C., Dee, D., and Thépaut, J.-N.: ERA5 hourly
935 data on pressure levels from 1940 to present, https://doi.org/10.24381/cds.bd0915c6, 2023.

Jennings, K. S., Winchell, T. S., Livneh, B., and Molotch, N. P.: Spatial variation of the rain-snow temperature threshold across the Northern Hemisphere, Nat Commun, 9, 1148, https://doi.org/10.1038/s41467-018-03629-7, 2018.

Jennings, K. S., Arienzo, M. M., Collins, M., Hatchett, B. J., Nolin, A. W., and Aggett, G.: Crowdsourced
940 Data Highlight Precipitation Phase Partitioning Variability in Rain‐Snow Transition Zone, Earth and Space Science, 10, https://doi.org/10.1029/2022EA002714, 2023.

Jeong, D. I. and Sushama, L.: Rain-on-snow events over North America based on two Canadian regional climate models, Climate Dynamics, 50, 303-316, https://doi.org/10.1007/s00382-017-3609-x, 2018.

945 Kneifel, S., Maahn, M., Peters, G., and Simmer, C.: Observation of snowfall with a low-power FM-CW K-band radar (Micro Rain Radar), Meteorology and Atmospheric Physics, 113, 75-87, https://doi.org/10.1007/s00703-011-0142-z, 2011.

Kochendorfer, J., Nitu, R., Wolff, M., Mekis, E., Rasmussen, R., Baker, B., Earle, M. E., Reverdin, A., Wong, K., Smith, C. D., Yang, D., Roulet, Y.-A., Buisan, S., Laine, T., Lee, G., Aceituno, J. L. C., Alastrué, J., Isaksen, K., Meyers, T., Brækkan, R., Landolt, S., Jachcik, A., and Poikonen, A.: Analysis of single-Alter-shielded and unshielded measurements of mixed and solid precipitation from WMO-SPICE, Hydrology and Earth System Sciences, 21, 3525-3542, https://doi.org/10.5194/hess-21-3525-2017, 2017.

Leroux, N. R., Vionnet, V., and Thériault, J. M.: Performance of precipitation phase partitioning methods and their impact on snowpack evolution in a humid continental climate, Hydrological Processes, 37, e15028, https://doi.org/10.1002/hyp.15028, 2023.

List, R. J.: Smithsonian meteorological tables, Smithsonian miscellaneous collections, 1951.

Locatelli, J. D. and Hobbs, P. V.: Fall speeds and masses of solid precipitation particles, Journal of Geophysical Research, 79, 2185-2197, https://doi.org/10.1029/JC079i015p02185, 1974.

Löffler-Mang, M., Kunz, M., and Schmid, W.: On the Performance of a Low-Cost K-Band Doppler Radar for Quantitative Rain Measurements, Journal of Atmospheric and Oceanic Technology, 16, 379-387, https://doi.org/10.1175/1520-0426(1999)016%3C0379:OTPOAL%3E2.0.CO;2, 1999.

Marks, D., Winstral, A., Reba, M., Pomeroy, J., and Kumar, M.: An evaluation of methods for determining during-storm precipitation phase and the rain/snow transition elevation at the surface in a mountain basin, Advances in Water Resources, 55, 98-110, https://doi.org/10.1016/j.advwatres.2012.11.012, 2013.

McGovern, A., Lagerquist, R., John Gagne, D., Jergensen, G. E., Elmore, K. L., Homeyer, C. R., and Smith, T.: Making the Black Box More Transparent: Understanding the Physical Implications of Machine Learning, Bulletin of the American Meteorological Society, 100, 2175-2199, https://doi.org/10.1175/BAMS-D-18-0195.1, 2019.

Muñoz Sabater, J.: ERA5-Land hourly data from 1950 to present, cds.e2161bac, 2019.

Musselman, K. N., Lehner, F., Ikeda, K., Clark, M. P., Prein, A. F., Liu, C., Barlage, M., and Rasmussen, R.: Projected increases and shifts in rain-on-snow flood risk over western North America, Nature Climate Change, 8, 808-812, https://doi.org/10.1038/s41558-018-0236-4, 2018.

Pierre, A., Jutras, S., Smith, C., Kochendorfer, J., Fortin, V., and Anctil, F.: Evaluation of Catch Efficiency Transfer Functions for Unshielded and Single-Alter-Shielded Solid Precipitation Measurements, Journal of Atmospheric and Oceanic Technology, 36, 865-881, https://doi.org/10.1175/JTECH-D-18-0112.1, 2019.

Rasmussen, R., Baker, B., Kochendorfer, J., Meyers, T., Landolt, S., Fischer, A. P., Black, J., Thériault, J. M., Kucera, P., Gochis, D., Smith, C., Nitu, R., Hall, M., Ikeda, K., and Gutmann, E.: How Well Are We Measuring Snow: The NOAA/FAA/NCAR Winter Precipitation Test Bed, Bulletin of the American Meteorological Society, 93, 811-829, https://doi.org/10.1175/BAMS-D-11-00052.1, 2012.

Rokach, L., Maimon, O., and Shmueli, E.: Machine Learning for Data Science Handbook, 3, Springer Cham, https://doi.org/10.1007/978-3-031-24628-9, 2023.

Ross, A., Smith, C. D., and Barr, A.: An improved post-processing technique for automatic precipitation gauge time series, Atmospheric Measurement Techniques, 13, 2979-2994, https://doi.org/10.5194/amt-13-2979-2020, 2020.

Sarkar, T., Das, S., and Maitra, A.: Assessment of different raindrop size measuring techniques: Inter-comparison of Doppler radar, impact and optical disdrometer, Atmospheric Research, 160, 15-27, https://doi.org/10.1016/j.atmosres.2015.03.001, 2015.

Shin, K., Kim, K., Song, J. J., and Lee, G.: Classification of Precipitation Types Based on Machine Learning Using Dual-Polarization Radar Measurements and Thermodynamic Fields, Remote Sensing, 14, 3820, https://doi.org/10.3390/rs14153820, 2022.

Singh, P., Spitzbart, G., Hübl, H., and Weinmeister, H. W.: Hydrological response of snowpack under rain-on-snow events: a field study, Journal of Hydrology, 202, 1-20, https://doi.org/10.1016/S0022-1694(97)00004-8, 1997.

Smith, C. D., Mekis, E., Hartwell, M., and Ross, A.: The hourly wind-bias-adjusted precipitation data set from the Environment and Climate Change Canada automated surface observation network (2001–2019), Earth System Science Data, 14, 5253-5265, https://doi.org/10.5194/essd-14-5253-202210.5194/essd-14-5253-2022, 2022.

Stewart, R. E.: Precipitation types in the transition region of winter storms, Bulletin of the American Meteorological Society, 73, 287-296, https://doi.org/10.1175/1520-0477(1992)073%3C0287:PTITTR%3E2.0.CO;2, 1992.

1005 Thériault, J. M. and Stewart, R. E.: A Parameterization of the Microphysical Processes Forming Many Types of Winter Precipitation, Journal of the Atmospheric Sciences, 67, 1492-1508, https://doi.org/10.1175/2009JAS3224.1, 2010.

Thériault, J. M., Stewart, R. E., and Henson, W.: On the Dependence of Winter Precipitation Types on Temperature, Precipitation Rate, and Associated Features, Journal of Applied Meteorology and Climatology, 49, 1429-1442, https://doi.org/10.1175/2010JAMC2321.1, 2010.

1010 Thorpe, A. and Mason, B.: The evaporation of ice spheres and ice crystals, British Journal of Applied Physics, 17, 541, 1966.

Wang, Y. H., Broxton, P., Fang, Y., Behrangi, A., Barlage, M., Zeng, X., and Niu, G. Y.: A Wet‐Bulb Temperature‐Based Rain‐Snow Partitioning Scheme Improves Snowpack Prediction Over the Drier Western United States, Geophysical Research Letters, 46, 13825-13835,
1015 https://doi.org/10.1029/2019GL085722, 2019.

Wayand, N. E., Stimberis, J., Zagrodnik, J. P., Mass, C. F., and Lundquist, J. D.: Improving simulations of precipitation phase and snowpack at a site subject to cold air intrusions: Snoqualmie Pass, WA, Journal of Geophysical Research: Atmospheres, 121, 9929-9942, https://doi.org/10.1002/2016JD025387, 2016.

1020 Wen, L., Nagabhatla, N., Lü, S., and Wang, S.-Y.: Impact of rain snow threshold temperature on snow depth simulation in land surface and regional atmospheric models, Advances in Atmospheric Sciences, 30, 1449-1460, https://doi.org/10.1007/s00376-012-2192-7, 2013.

Wever, N., Würzer, S., Fierz, C., and Lehning, M.: Simulating ice layer formation under the presence of preferential flow in layered snowpacks, The Cryosphere, 10, 2731-2744,
1025 https://doi.org/10.5194/tc-10-2731-2016, 2016.

WMO: 6.1.2 Units and scales, in: Measurement of Meteorological Variables, 2023 edition ed., Guide to instruments and methods of observation, Volume 1, WMO, Geneva, 574, 2018.

Yau, M. K. and Rogers, R. R.: A short course in cloud physics, Third Edition, Elsevier, 1996.

Ye, H., Cohen, J., and Rawlins, M.: Discrimination of Solid from Liquid Precipitation over Northern Eurasia
1030 Using Surface Atmospheric Conditions*, Journal of Hydrometeorology, 14, 1345-1355, https://doi.org/10.1175/JHM-D-12-0164.1, 2013.

Ye, H., Yang, D., and Robinson, D.: Winter rain on snow and its association with air temperature in northern Eurasia, Hydrological Processes, 22, 2728-2736, https://doi.org/10.1002/hyp.7094, 2008.

1035

12   Figures
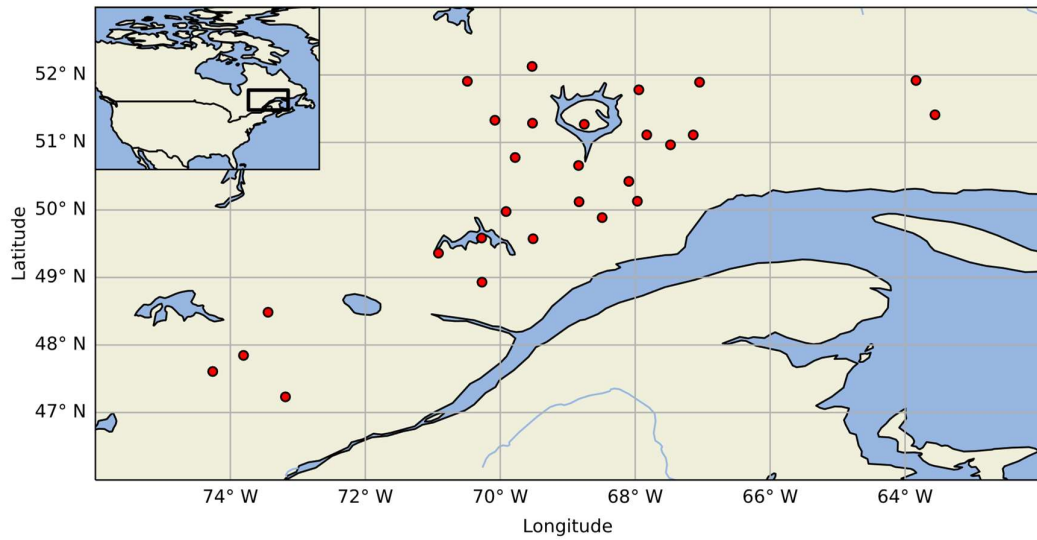
Figure 1: Location of the study sites in eastern Canada. The black square in the top left inset corresponds to
1040   **the map domain.**
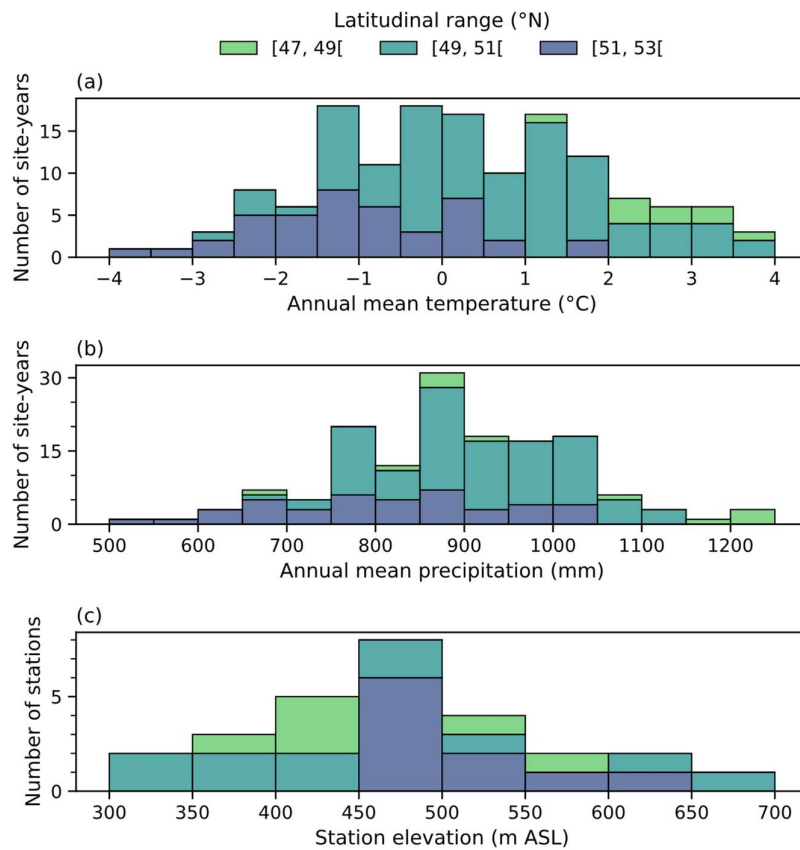
Figure 2: Distributions of the (a) annual mean temperature, (b) annual mean precipitation and (c) elevation at the study sites, separated by latitudinal range.
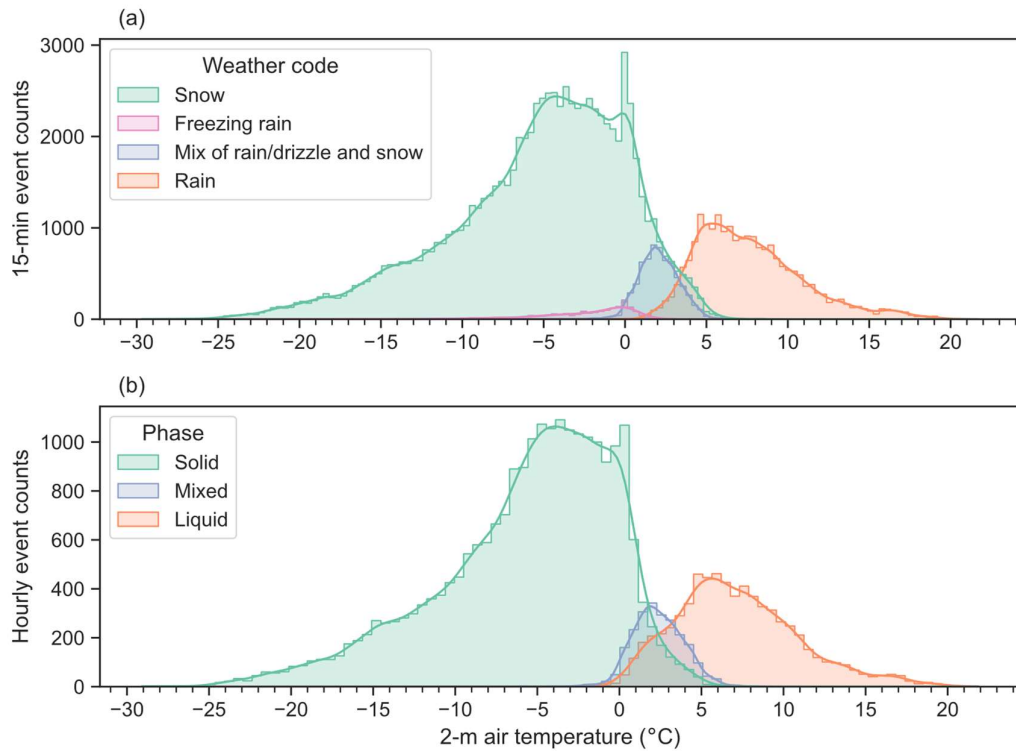
Figure 3: Event counts of (a) the 15-min precipitation phase identified by the disdrometers and (b) the aggregated hourly precipitation phases according to the 2-m air temperature.
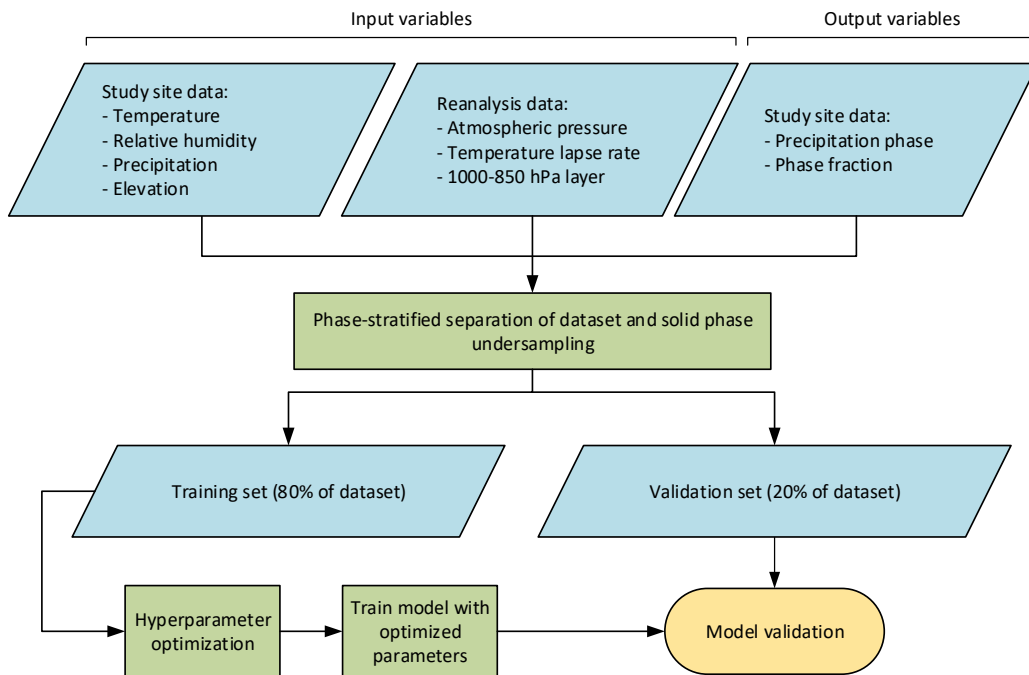
Figure 4: Development and validation methodology for the Phase-Guided-Partitioning model.
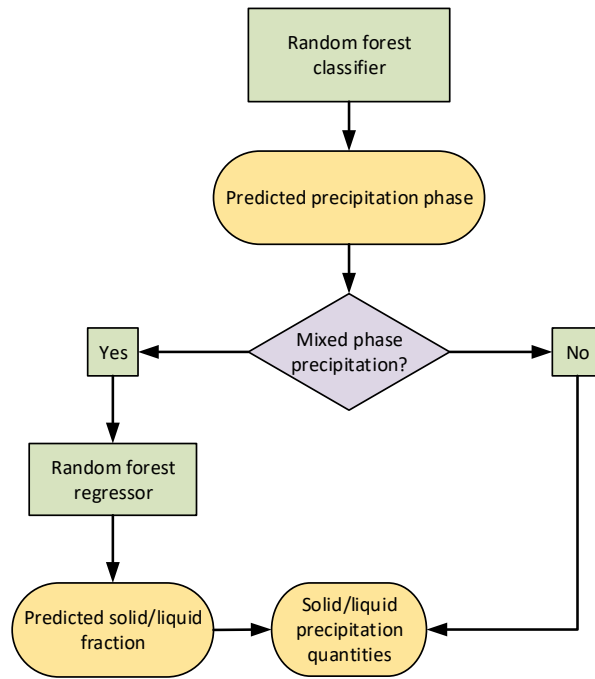
 Figure 5: Phase-Guided-Partitioning model structure.
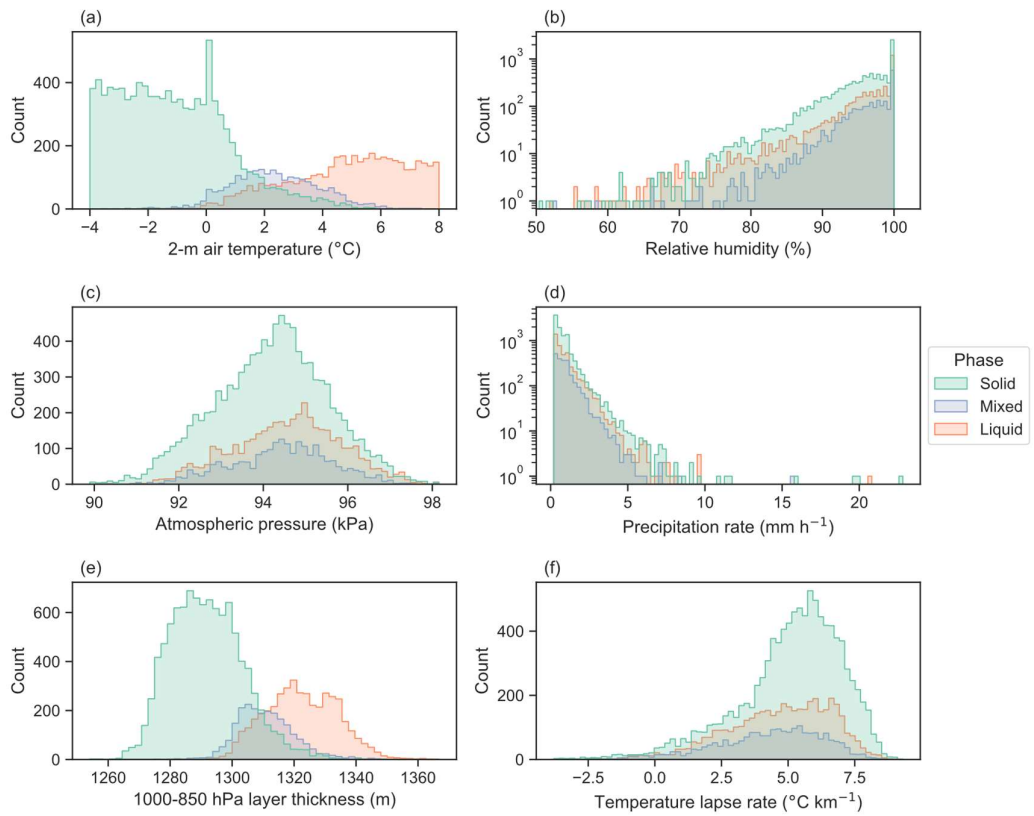
Figure 6: Input distributions separated by phase of (a) 2-m air temperature, (b) relative humidity, (c) atmospheric pressure, (d) precipitation rate, (e) 1000-850 hPa layer thickness, (f) air temperature lapse rate.
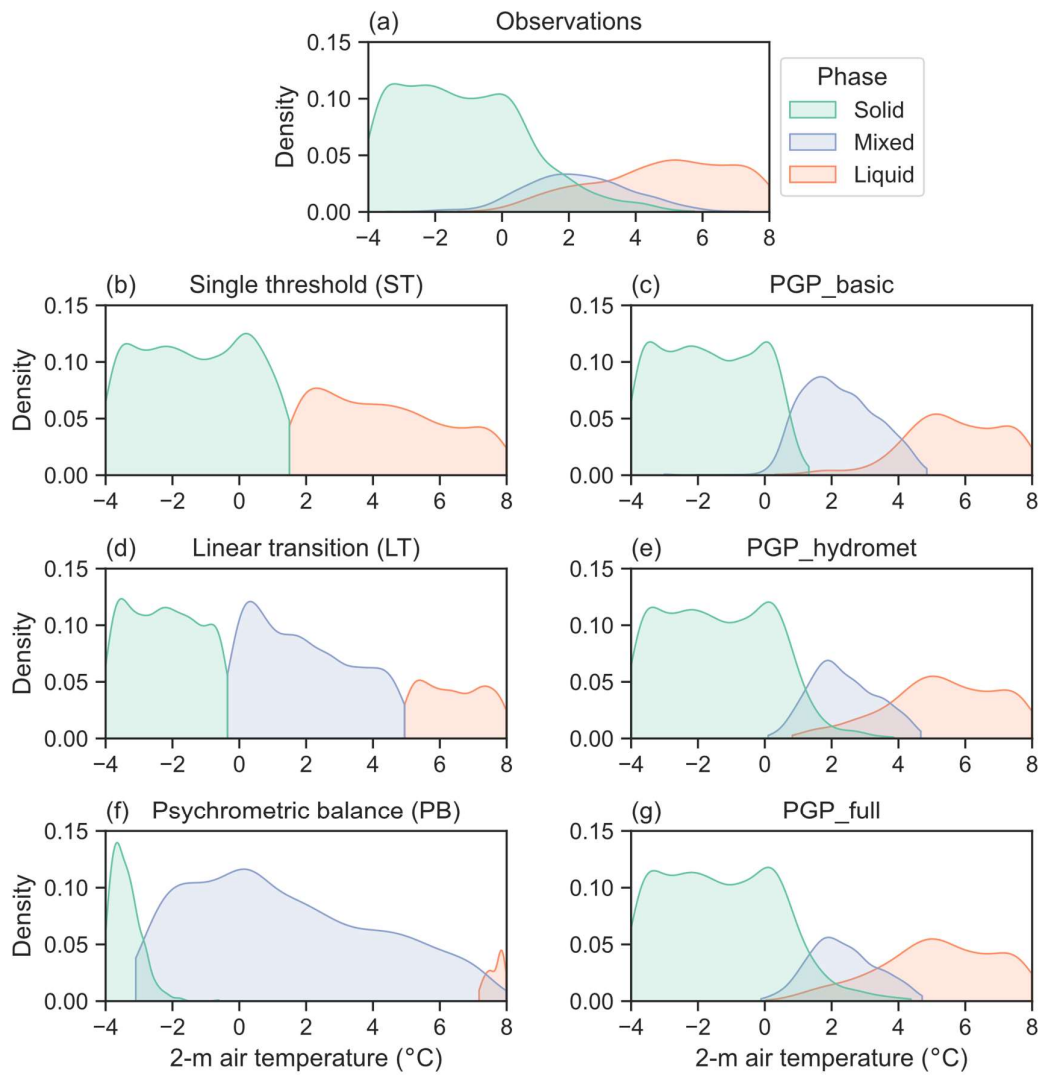
Figure 7: Hourly phase distributions according to 2-m temperature of the (a) observations, (b) single threshold, (c) PGP_basic, (d) linear transition, (e) PGP_hydromet, (f) psychometric balance and (g) PGP_full. PGP model details are summarized in Table 2.

1055
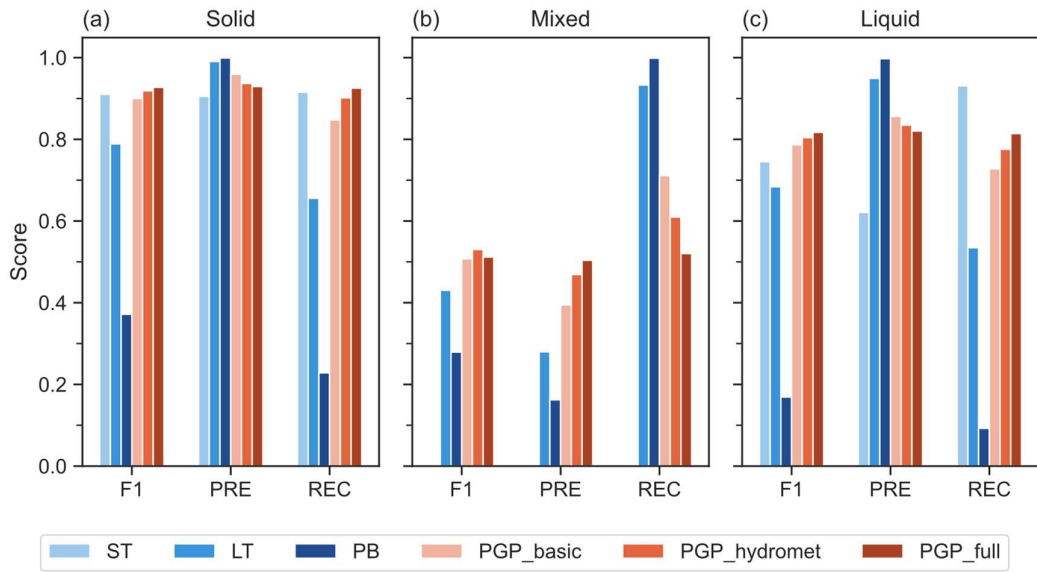
Figure 8: Model phase classification metrics separated by (a) the solid, (b) the mixed and (c) the liquid phase. PGP model details are summarized in Table 2.
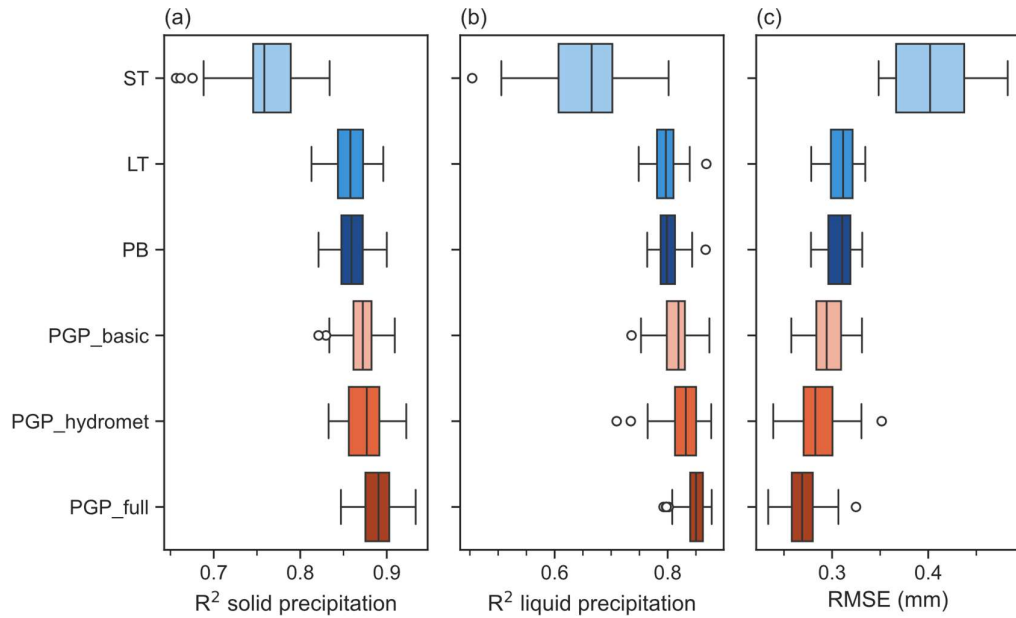
Figure 9: Model regression performance in (a) R^2 for solid precipitation, (b) R^2 for liquid precipitation and (c) RMSE. PGP model details are summarized in Table 2.
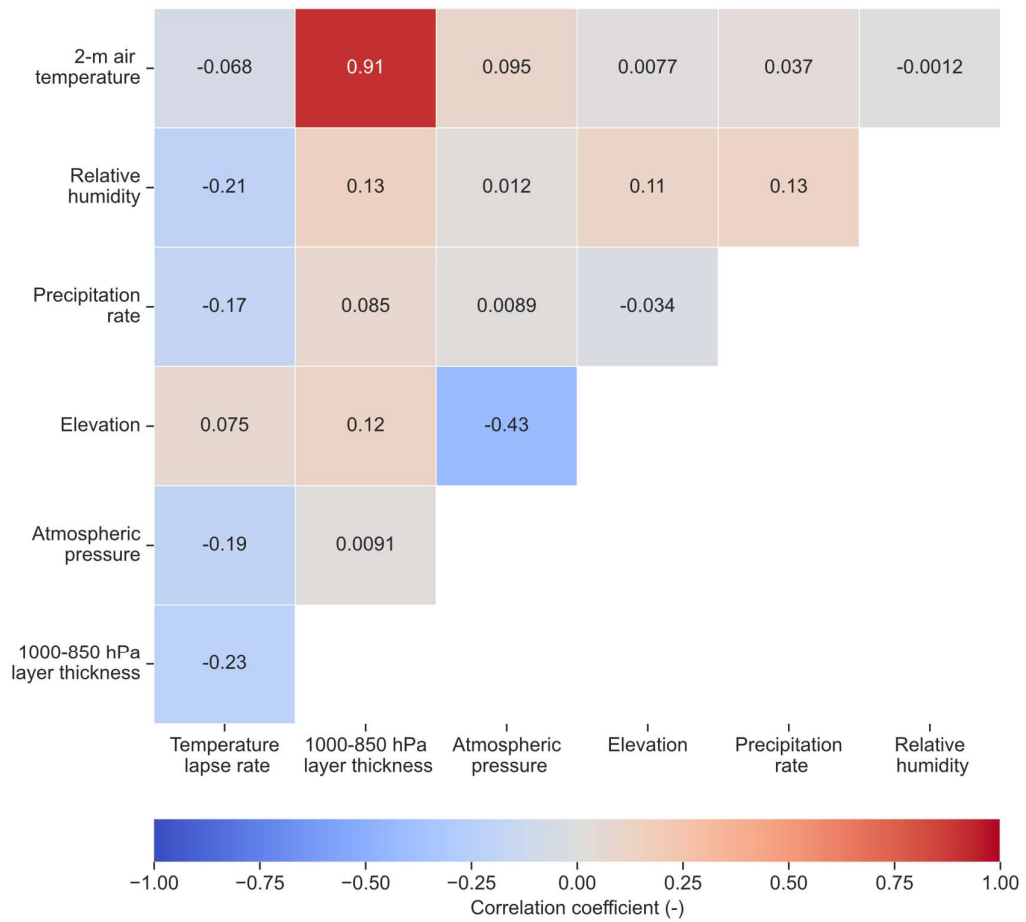
Figure 10: Correlation matrix of PGP_full input variables pairs.
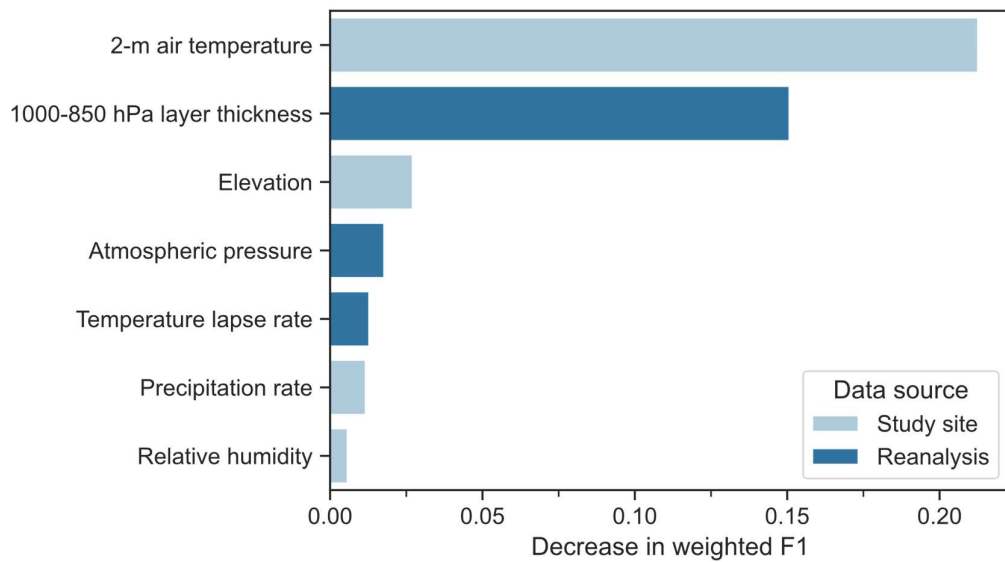
Figure 11: Permutation importance of PGP_full input variable, showing the decrease in the model's weighted F1 score.
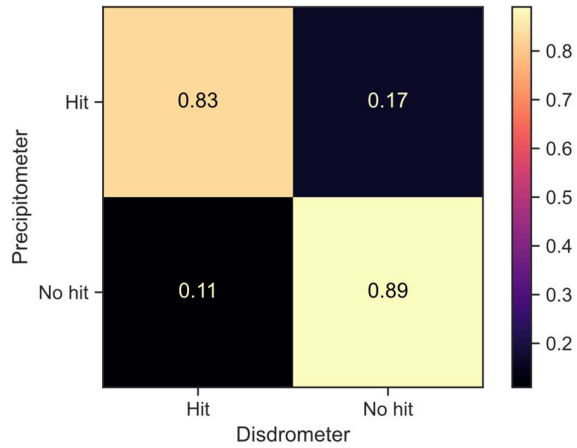
1070   **Figure 12: Confusion matrix of the precipitometers and disdrometers 15-min precipitation hit-rate, normalized over the precipitometer observations. The upper-left metric is the probability of detection, upper-right metric is the miss rate, and the lower-left metric is the false alarm rate.**
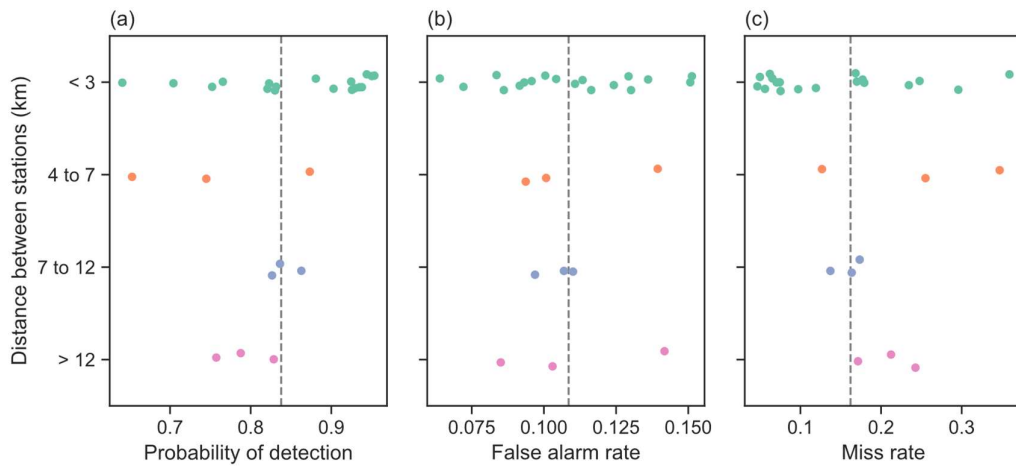
Figure 13: Comparison of the (a) Probability of detection, (b) false alarm rate, and (c) miss rate according to
1075   **the distance between the study site and paired weather stations. The dashed grey line corresponds to the metric computed on the full dataset in Figure 12.**
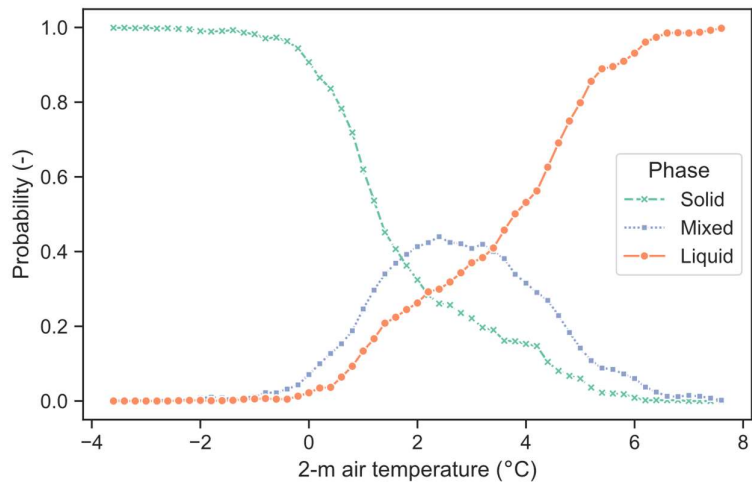
Figure 14: Observed probability of occurrence for the solid, liquid, and mixed phase.
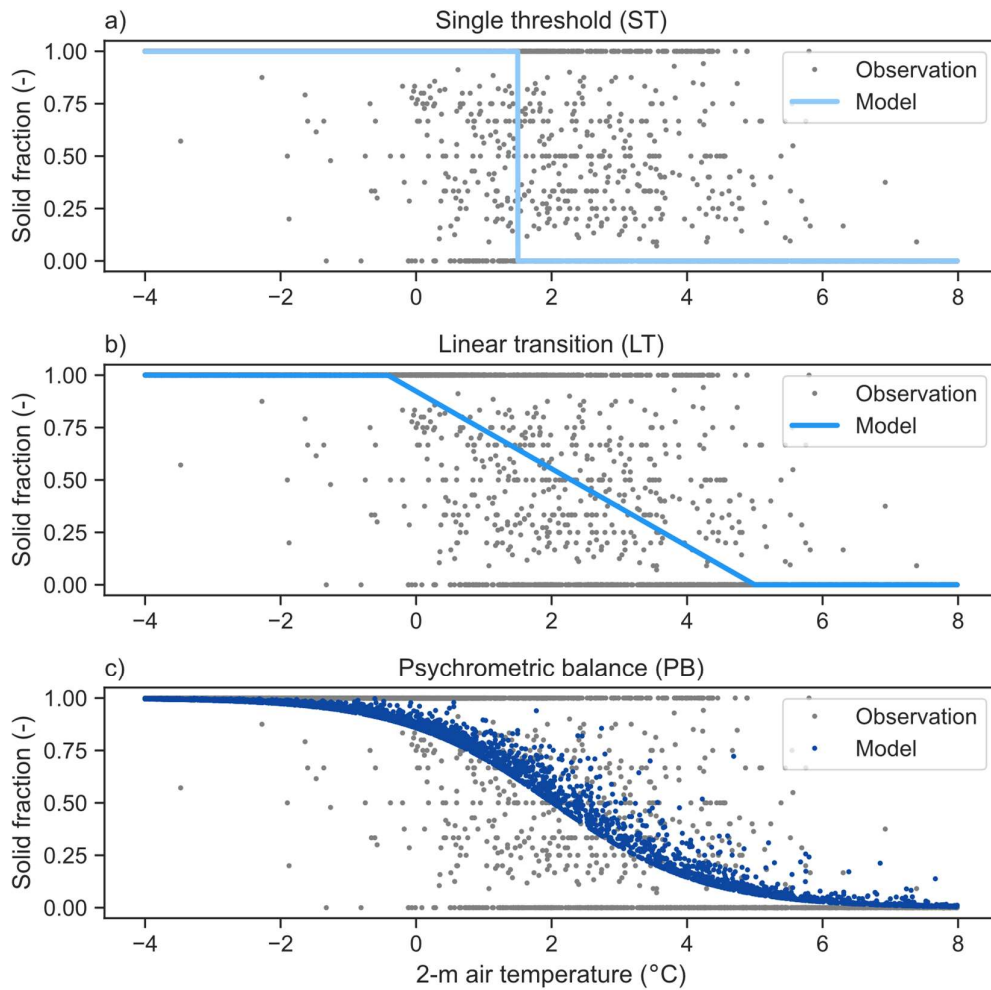
1080   **Figure C1: Observed solid precipitation fraction according to the 2-m air temperature and the modelled solid precipitation fraction of the (a) static threshold, (b) linear transition and (c) psychrometric balance.**

13 Tables

Table 1: Study site instruments details.

Model, manufacturer	Temporal resolution	Observation	Specifications
WS100, Lufft	15 min	Precipitation phase	See section 3.1 and Appendix B.
Pluvio^2, OTT	15 min	Precipitation rate	Resolution: 0.1 mm Accuracy: ±0.05 mm
CS109, Campbell Scientific	60 min	Near-surface air temperature	Accuracy: ±0.2°C (from 0°C to 70°C), increasing to ±0.5°C at −50°C
HMP155a, Campbell Scientific	60 min	Near-surface relative humidity	Accuracy: ±(1.0 + 0.008 × reading) % RH (from −20°C to 40°C)
05103, R.M. Young	15 min	Wind speed 2 m above ground	Wind speed threshold: 1.0 m s^{-1} Accuracy: ±0.3 m s^{-1}
SR50A, Campbell Scientific	60 min	Snowpack depth	Resolution: 0.25 mm Accuracy: ±1 cm or 0.4% of distance to target
CS725, Campbell Scientific	6 h	Snowpack SWE	Resolution: 1 mm Accuracy: ±15 mm (from 0 mm to 300 mm)

1085 **Table 2: Listing of the input variables used in the tested PGP models.**

PGP model	Input variables
PGP_basic	2-m air temperature, elevation
PGP_hydromet	2-m air temperature, elevation, relative humidity, atmospheric pressure, precipitation rate
PGP_full	2-m air temperature, elevation, relative humidity, atmospheric pressure, precipitation rate, 1000-850 hPa layer thickness, temperature lapse rate

Table 3: Weighted classification scores for Single Threshold (ST), Linear Transition (LT), Psychrometric Balance (PB) and Phase-Guided Partitioning PGP models. PGP model details are summarized in Table 2.

Model	F1	Precision	Recall
ST	0.74	0.71	0.79
LT	0.71	0.88	0.66
PB	0.31	0.88	0.30
PGP_basic	0.82	0.86	0.80
PGP_hydromet	0.84	0.85	0.83
PGP_full	0.84	0.84	0.84

1090

Table 4: Average regression scores for Single Threshold (ST), Linear Transition (LT), Psychrometric Balance (PB) and Phase-Guided Partitioning (PGP) models. PGP model details are summarized in Table 2.

Model	R^2 solid	R^2 liquid	RMSE (mm)
ST	0.76	0.65	0.40
LT	0.86	0.80	0.31
PB	0.86	0.80	0.31
PGP_basic	0.87	0.81	0.30
PGP_hydromet	0.88	0.83	0.29
PGP_full	0.89	0.85	0.27

 Table A1: List of study site coordinates, elevation, and timeframes when the station has been in operation.

Station name	Longitude (° W)	Latitude (° N)	Elevation (m ASL)	Operational timeframe
ARGENT	69.778857	50.776574	641	2020-2023
AUXLOUPS	70.487430	51.905890	537	2020–2023
BAUBERT	63.556960	51.409460	541	2020-2022
BETSIA_M	69.913268	49.976570	403	2019-2023
CABITUQG	69.513611	49.573333	491	2019-2023
CONRAD	74.261131	47.607249	433	2020-2023
DIAMAND	73.183080	47.231302	373	2020-2023
GAREMANG	67.139860	51.110640	778	2020-2023
HARTJ_G	67.945980	51.779310	460	2020-2023
LACROI_G	70.079390	51.328710	621	2019-2023
LAFLAM_G	70.270496	48.930225	519	2019-2023
LBARDO_G	67.828433	51.111896	486	2019-2023
LEVASSEU	68.754960	51.268480	466	2020-2023
LOUIS	68.489740	49.886620	315	2020-2023
LOUISE_G	68.839767	50.658526	397	2019-2023
MOUCHA_M	69.527780	52.125510	565	2019-2022
NOIRS	68.831730	50.121160	385	2020-2023
PARLEUR	69.522370	51.285470	485	2020-2021
PERDRIX	67.967450	50.129460	315	2022-2023
PIPMUA_G	70.915810	49.360520	566	2020-2023
PORTO	70.275910	49.584230	413	2020-2023
ROUSSY_G	68.094360	50.423470	456	2020-2023
RTOULNUS	67.476760	50.964750	688	2020–2022
SAUTEREL	63.838040	51.917820	459	2020–2023
STMARG_G	67.046360	51.891980	461	2020–2023
WABISTAN	73.441157	48.484572	565	2020–2023

Table B1: Precipitation events characteristics separated by phase.

Main phase	Event count	Mean temperature (°C)	ΔSWE (mm)	ΔSD (cm)
Snow	192	-2.0	3.0	3.3
Rain	12	3.6	3.5	-1.8
Mix of rain/drizzle and snow	19	1.5	5.9	-1.5
Freezing rain	12	-1.7	3.2	0.2

1100

Table C1: Benchmark model calibrated parameters.

Model	Calibrated parameters
Single threshold (ST)	$T_K = 1.50$
Linear transition (LT)	$T_{snow} = -0.38$ $T_{rain} = 5.00$
Psychrometric balance (PB)	$b = 6.34$ $c = 0.39$